

Time-resolved evolution of micro-discharges, surface ionization waves and plasma propagation in a two-dimensional packed bed reactor

Kenneth W Engeling^{1,3} , Juliusz Kruszelnicki¹, Mark J Kushner²  and John E Foster¹ 

¹ University of Michigan, Dept. of Nuclear Engineering and Radiological Sciences, 2355 Bonisteel Boulevard, Ann Arbor, MI 48109-2104, United States of America

² University of Michigan, Dept. of Electrical Engineering and Computer Science, 1301 Beal Avenue, Ann Arbor, MI 48109-2122, United States of America

E-mail: kenengel@umich.edu, jkrusze@umich.edu, mjkush@umich.edu and jefoster@umich.edu

Received 6 March 2018, revised 28 May 2018

Accepted for publication 11 July 2018

Published 1 August 2018



CrossMark

Abstract

Plasma packed bed reactors (PBRs) are being investigated for applications ranging from pollution remediation to chemical synthesis, including plasma catalysis. Plasma PBRs typically operate as dielectric barrier discharges where the plasma propagating through the PBR strongly interacts with the dielectric packing media and gas in the interstitial spaces. The nature of plasma propagation through this macroscopically porous-like medium is not well understood. Plasma formation in PBRs is a function of many parameters, including dielectric media composition and surface morphology, dielectric constant, packing fraction, pressure, and the applied voltage waveform. Imaging the plasma propagation through the complex three-dimensional geometry of the packing media and interstitial spaces that make up the PBR is difficult to experimentally execute. In this regard, a two-dimensional PBR composed of dielectric disks was developed to enable optical imaging of plasma formation and propagation. The mode of plasma propagation and the sensitivity of discharge formation to material dielectric constant, applied voltage, and pressure were experimentally and computationally investigated. We found that higher dielectric constants of the packing material produced more intense, localized filamentary micro-discharges between disks. In general, plasma propagation through the PBR at 1 atm is initiated by localized micro-discharges between adjacent dielectric disks, which in turn give rise to surface ionization waves (SIWs) that propagate along the dielectric surface. At pressures below 1 atm, the discharge was more diffuse regardless of the dielectric media, filling the interstitial space instead of forming SIWs.

Keywords: dielectric barrier discharge, packed bed reactor, micro-discharge, surface ionization wave, atmospheric pressure plasma

1. Introduction

Remediation of toxic gases, chemical gas conversion, ozone generation, and plasma catalysis are examples of atmospheric pressure plasma applications which utilize dielectric barrier

discharges (DBDs) [1]. The packed bed reactor (PBR) is one form of a DBD that is particularly promising for chemical conversion processes due to its high energy efficiency and chemical selectivity, particularly when used in concert with catalysts [1–9]. A PBR in its simplest form consists of two electrodes, powered and grounded, whose intervening gap is filled with dielectric media, typically spherical beads [4].

³ Author to whom any correspondence should be addressed

Under select conditions, surface ionization waves (SIWs) propagate over the dielectric beads, whose high intensity improves remediation efficiency [1].

The dielectric material in PBRs can also enhance the electric field in the gaps between the dielectric media, which facilitates electrical breakdown in those regions. This enhancement depends upon the geometrical layout and dielectric constant of the packing media [2, 4]. Electric field enhancement is more pronounced for pointed, irregularly shaped media in contrast to a smooth, rounded surface, though natural polarization of even spherical beads leads to electric field enhancement at the poles of the beads aligned with the applied electric field. (Applied electric field results from the applied potential, geometry and material properties in the absence of the plasma.) Electric field enhancement also occurs along the curved surfaces of dielectric media in PBRs, leading to the formation of SIWs similar to those found in DBDs. In parallel plate DBDs, the applied electric field is generally perpendicular to the direction of propagation of SIWs, which can limit the intensity of the SIWs. Since the applied electric field may have a component parallel to the direction of propagation of SIWs in PBRs, the SIWs can be more intense than in DBDs. Given the broad parameter space in which PBRs can operate (e.g., geometry, materials, voltage waveforms), predicting the sensitivity of plasma properties to the variation of such parameters is difficult.

The packing fraction of a PBR, defined as the ratio of the volume of the dielectric aggregate to the total reactor volume, determines the void volume and is therefore a measure of aggregate porosity. The void fraction is a measure of the maximum volume in which plasma can form in the PBR. The ratio of the surface area that surrounds the void to the volume of the void is also important, affecting both surface and volume production of reactants [10]. Butterworth *et al* investigated the consequences of dielectric particle size, and packing fraction in PBRs for CO₂ reduction. They found that an optimum particle size maximized the chemical reactivity produced by the plasma [11]. They investigated barium titanate (BaTiO₃) and alumina (Al₂O₃) dielectric particle sizes of 180–300 μm, 300–500 μm, 500–850 μm, 850–1400 μm, and 1400–2000 μm. (Particle shapes were random.) Discharge formation was possible with every particle size however the smallest size range, which also had the highest packing fraction, produced the highest rate of conversion. Numerous micro-discharges occurred dispersed throughout PBR with BaTiO₃ ($\epsilon_r = \epsilon/\epsilon_0 \approx 4000$). With Al₂O₃ ($\epsilon_r \approx 10$) aggregate, long streamers propagated through the media.

Chung *et al* investigated the influence of dielectric constant on the efficiency of dry reforming of methane using DBDs and ferroelectric PBRs [1]. The dielectric media consisted of glass beads having $\epsilon_r = 3$ –5, BaZr_{0.75}Ti_{0.25}O₃ (BZT) with $\epsilon_r = 149$, and BaFe_{0.5}Nb_{0.5}O₃ (BFN) with $\epsilon_r = 2025$. For an applied voltage of 12.6 kV, the power deposition was 16–20 W with a small sensitivity to dielectric constant. However the morphology and spatial distribution of the plasma was a function of the dielectric constant. For example, for higher dielectric constant material, the plasma discharges

were localized and intense, as also observed in the single pellet discharge experiments by Butterworth and Allen [12]. Michielsen *et al* also investigated the consequences of particle size and dielectric constant for CO₂ dissociation in a packed bed DBD reactor [13]. They attributed trends in conversion and energy efficiency to bead size and material properties. Mei *et al* concluded that the presence of BaTiO₃ or glass beads in a cylindrical DBD reactor also affected the morphology of the plasma [14]. In that work, a combination of filamentary and surface discharges occurred. Van Laer and Bogaerts computationally investigated the sensitivity of PBRs to the diameter of dielectric beads and dielectric constant [15]. Their simulations demonstrated the effect of electric field enhancement resulting from increasing dielectric constant on plasma production. At high dielectric constants, discharges tended to be localized between beads rather than propagating through channels. With low dielectric constants, the plasma filled the volume of the interstitial cavities.

Kang *et al* experimentally and numerically investigated surface streamer propagation over alumina beads in PBRs, and found average streamer velocities of about $2.5 \times 10^7 \text{ cm s}^{-1}$ [16]. The velocity moderately increased with applied. Wang *et al* investigated streamer propagation in a PBR intended for plasma catalysis [17]. Their calculations indicated that DBD reactors may exhibit three types of discharge behavior—positive restrikes, filamentary micro-discharges, and SIWs [18].

The manner in which plasma power is spatially distributed and in what form (e.g., micro-discharges or SIWs) as a function of dielectric constant, media size and arrangement in PBRs is not well understood. Controlling the discharge morphology and mode of propagation are critical to optimizing of PBRs for plasma catalysis and other applications where surface reactions are important. In this paper, we discuss results from experimental and computational investigations of plasma formation and propagation in an idealized, two-dimensional (2D) PBR reactor sustained in air at atmosphere and sub-atmospheric pressures to as low as 10 Torr. Plasma morphology and propagation were investigated using fast-camera imaging and a 2D computational model. In general, imaging plasma propagation in a conventional PBR is difficult owing to line-of-sight obstruction from intervening dielectric aggregate. To circumvent this problem, a 2D-PBR was constructed, consisting of a single 2D layer of dielectric disks (quartz or zirconia) in a hexagonal array. Using a microscope and macro-lens combination, the 2D apparatus enabled imaging of local micro-discharge formation between disks and macroscopic plasma propagation throughout the array.

The experimental setup and procedures are described in section 2.1 and the computational model is described in section 2.2 2D-PBR imaging as a function of dielectric constant is discussed in section 3. The effect of pressure on discharge morphology and propagation is discussed in section 4 followed by a discussion of computational results in section 5. Concluding remarks are in section 6.

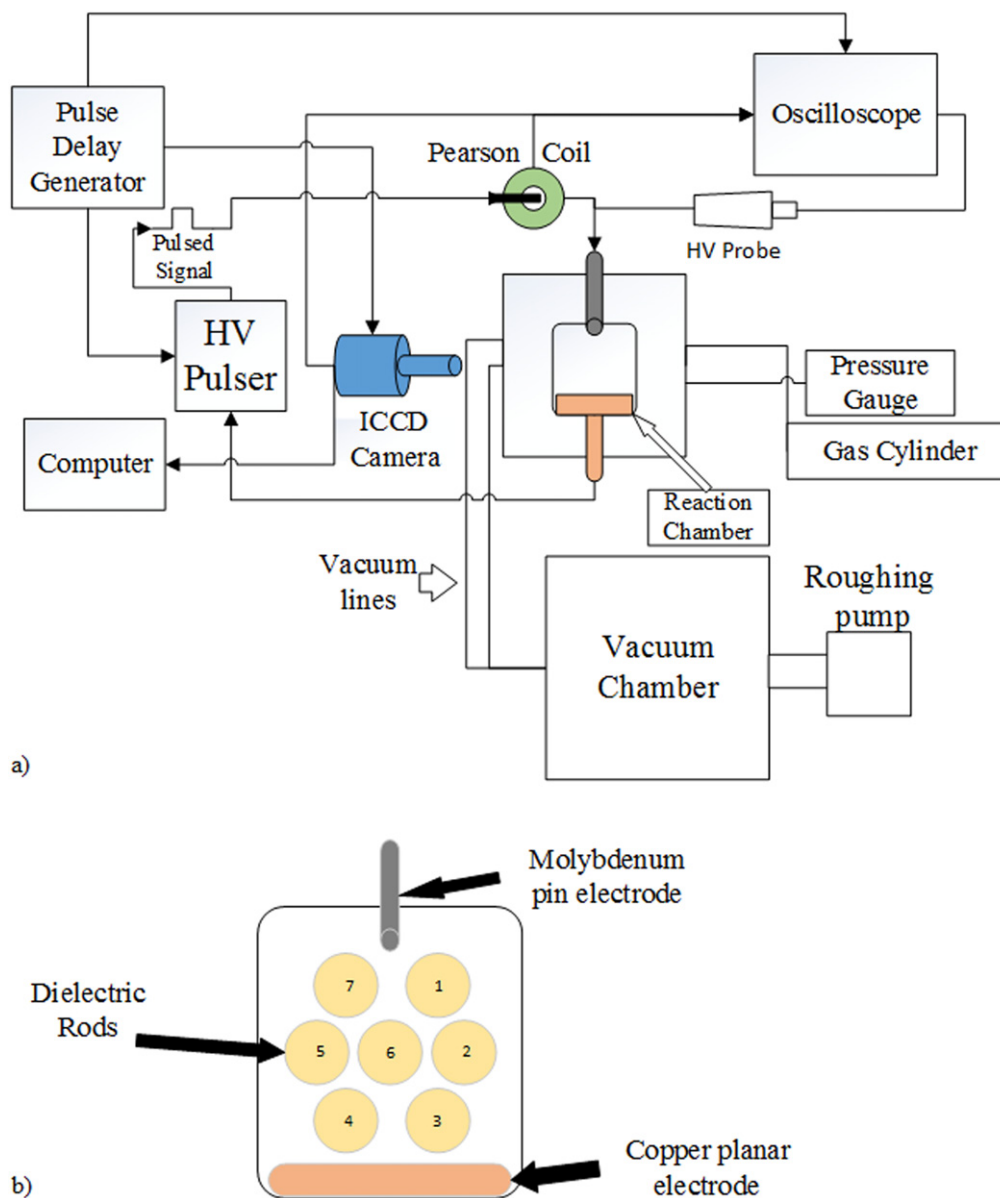


Figure 1. Experimental setup for the time-resolved micro-discharge imaging. (a) Schematic of apparatus. (b) Top-view of reaction chamber with media.

2. Description of the experiment and model

2.1. Experiment

Schematics of the experimental apparatus and 2D-PBR are in figure 1. The plasma is sustained sandwiched between two quartz plates 6.35 mm in thickness. One plate contains a recessed area to accommodate the dielectric disks which make the PBR and the electrodes. Seven dielectric disks of quartz (5 mm in diameter and 3 mm thick) or zirconia (6.2 mm in diameter and 3.5 mm thick) were sandwiched into this quartz plate assembly. These diameters and thicknesses were the closest matches commercially available for the two materials. While the quartz and zirconia disks are different sizes, the main interest was investigating the consequences of dielectric constant. Simulations showed that the difference in electric field enhancement

resulting from the different sizes was less than 5%. For example, for the quartz beads, the maximum electric field increased from 1.75×10^4 to 1.83×10^4 kV cm⁻¹.

The hexagonal array of dielectric material, whose span was 20 mm, was located between two metal electrodes configured in a pin-to-plane configuration. The pin electrode having a 2 mm diameter was molybdenum and the planar electrode (25 mm wide \times 4 mm depth) was copper. The spacing, thickness and orientation of the dielectric disks were chosen so that the discharge propagated through the array of disk touching their edges rather than over the top or bottom of the disks. In this manner, the discharge is limited to a single plane. The quartz disks have a relative dielectric constant of $\epsilon_r = 3.8$. The dielectric properties of the zirconia disks were characterized by the resonant post technique described elsewhere [19, 20]. The measured relative

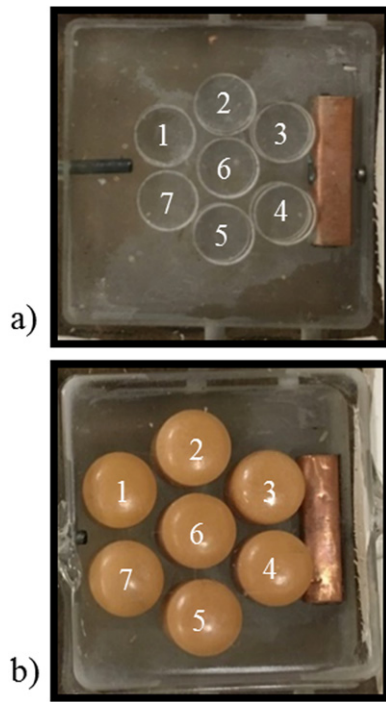


Figure 2. Hexagonal pattern of dielectric disks in a pin-to-plane electrode configuration. (a) Quartz (5 mm diameter), (b) zirconia (6.1 mm diameter).

dielectric constant for the zirconia disks was $\epsilon_r = 26.6 \pm 0.24$ at 6.2 GHz.

Dielectric disks were placed in a hexagonal configuration as shown in figure 2. (The disks are not in contact with the electrodes.) For the quartz disks the average center to center spacing was 6 mm with a minimum gap of ≈ 1 mm, producing a void fraction of 22%. For the zirconia disks, the center to center spacing was 7.2 mm also with a minimum separation of ≈ 1 mm, producing a void fraction of 30%. In 2D, gaps are required between the disks to enable propagation of the discharge through the array. The hexagonal configuration mimics the highest packing fraction layout of spherical beads in a 3D PBR. In 3D PBRs, the beads are typically in contact, which produces larger electric field enhancement adjacent to the contact points than will occur in the 2D-PBR [15]. As a result, the intensity of the microdischarges in the 2D-PBR are likely less than will be found in 3D PBRs.

The geometrical placement of the dielectric disks determines the initial spatial distribution of E/N (reduced electric field: electric field/gas density) in the gaps between the disks [8, 11, 21]. For example, vacuum electric fields are shown in figure 3 for the 2D-PBR with quartz and zirconia disks for an applied voltage of 20 kV. The electric field was calculated by solving Poisson's equation using ANSYS Maxwell, a commercial software package. Electric field enhancements naturally occur at the poles of the disks due to polarization of the dielectric. Electric field enhancement also occurs in the gaps between disks due to the reduction of electric field inside the high dielectric constant disks, which increases the voltage drop and electric field in the gaps predicted by ANSYS Maxwell simulations for the vacuum field. (When plasma is

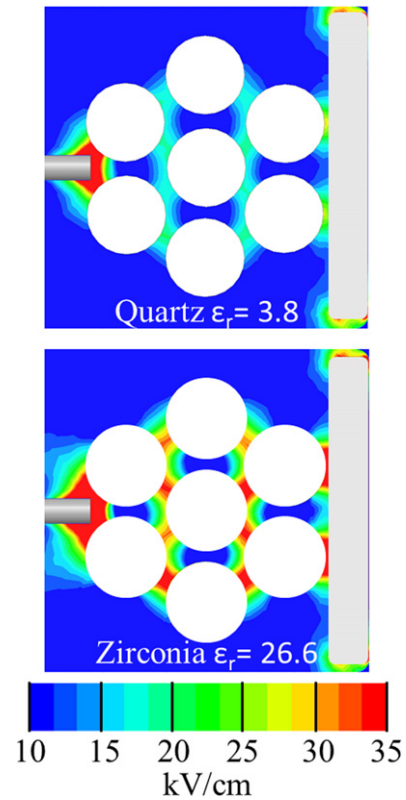


Figure 3. Calculated electric field for applied voltage of 20 kV in the 2D-PBR for (top) quartz ($\epsilon_r/\epsilon_0 = 3.8$) and (bottom) zirconia ($\epsilon_r/\epsilon_0 = 26.6$).

active, *nonPDPSIM* is used.) Although additional field enhancement may also occur due to surface roughness, the disks in this study were relatively smooth, with a roughness on the order of few tens of microns.

The pin electrode was biased with an isolated output, high voltage pulse generator (Eagle Harbor Technologies Nanosecond Pulser-120 (EHT NSP-120)) as shown in figure 1(a). The voltage pulse used for experiments at 1 atm had a peak amplitude of 20 kV and a pulse-width of 120 ns. For sub-atmospheric pressure experiments (200–10 Torr), 12 kV, 120 ns wide pulses were used. A Tektronix P6015A High voltage probe was used to measure voltage. A current transformer (Pearson Model 6585) was used with a Tektronix MDO 3024 Mixed Domain Oscilloscope to measure current. The discharge was imaged with an Andor iStar ICCD camera fitted with a microscope lens of $2.5\times$ magnification that captured images with a 5 ns integration time. The discharges were single shot with each image corresponding to a single applied voltage pulse. Using a delay generator, the position of the ICCD camera's trigger pulse relative to the time of application of the high voltage pulse was adjusted; thereby facilitating time resolved imagery, albeit using separate pulses. The initial time, $t = 0$, is the instant at which the power supply delivers voltage to the electrodes, which occurs ≈ 335 ns after the power supply is triggered as there is an inherent time delay in the power supply and cables.

Images were acquired on successive discharge pulses with additional delays of 5 ns to generate a time sequence of

discharge formation. This process proceeded until emission from the cell was no longer distinguishable from the background. The $2.5\times$ magnification lens provided a resolution of $5.6\ \mu\text{m}/\text{pixel}$. A macro lens providing a resolution of $127\ \mu\text{m}/\text{pixel}$ was used to study discharge propagation over the entirety of the dielectric array. The camera was enclosed in a Faraday cage to minimize electromagnetic interference generated by the power supply and discharge.

For the 1 atm experiments, the test cell was left vented to the ambient. For the low pressure studies, the system was sealed with an elastomer gasket and connected via stainless steel tubing to a large vacuum chamber. A precision leak valve located between the reactor and the vacuum chamber allowed for control of pressure in the test cell, which was monitored using an Inficon PCG 550 capacitance manometer.

2.2. Model

Modeling of the 2D-PBR was performed using the 2D multi-fluid simulator *nonPDPSIM* [21, 22]. This computational platform addresses charged particle, neutral and radiation transport, and plasma-surface interactions. Poisson's equation is implicitly integrated simultaneously with the continuity equations for charged species and surface charge density over an unstructured mesh. The electron temperature is calculated by solving the electron energy equation, while the electron reaction rate coefficients and transport coefficient are derived from local solutions to the Boltzmann's equation for the electron energy distribution. Radiation transport is included by applying a Green's function that describes the emission and absorption of ionizing radiation from each node to other nodes within the line-of-sight. All ions were assumed to neutralize on surfaces and return to the plasma as their neutral counterparts. Secondary electron emission from dielectric surfaces was accounted for with the emission coefficient of $\gamma_{SE} = 0.1$. Electrons uniformly stick to all surfaces or recombine with positive charge on those surfaces. This results in charging of the surface of dielectric materials, which is then included in the solution of Poisson's equation.

The humid air reaction mechanism includes 33 species and 143 reactions and is a subset of the mechanism first described by Dorai *et al* [23]. The reactions include 39 electron-impact processes with the remainder representing reactions between heavy particles. The charged particle reactions include ion-ion neutralization, electron detachment, charge exchange, electron-ion recombination and associative charge exchange leading to terminal species of water-cluster ions. Neutral reactions lead to formation of N_xO_y species, hydrogen peroxide, and ozone as terminal species on the time scales addressed here. All excited states are quenched on surfaces. The radiation transfer model includes emission of VUV photons from nitrogen singlets [$\text{N}_2(\text{b}^1\Pi)$ and $\text{N}_2(\text{b}^1\Sigma)$]. The cross-sections used for radiation transport were $1 \times 10^{-18}\ \text{cm}^2$ for non-ionizing absorption by O_2 and N_2 , $3 \times 10^{-17}\ \text{cm}^2$ for non-ionizing absorption by H_2O , and $1 \times 10^{-19}\ \text{cm}^2$ for photo-ionization of O_2 .

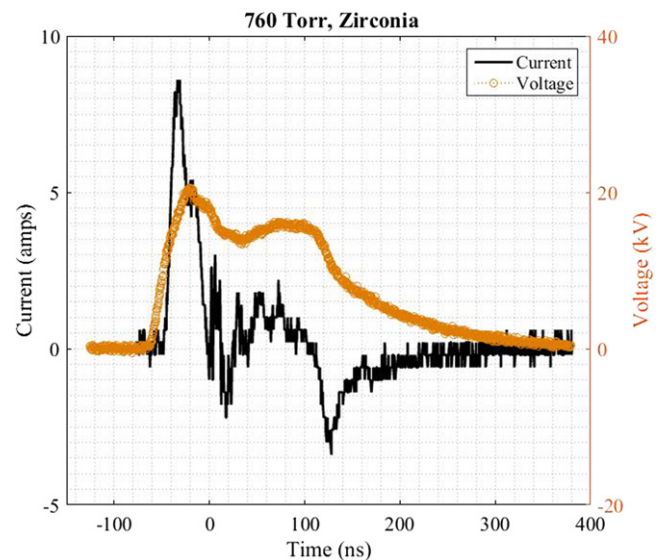


Figure 4. Electrical waveforms with zirconia disks for a discharge at 760 Torr. (Black) current and (orange) voltage.

3. Discharge evolution at atmospheric pressure

The evolution of the discharge in the 2D-PBR after each initiating voltage pulse was imaged in 5 ns increments by adjusting the delay in the trigger pulse to the camera. The minimum exposure time required to capture sufficient light over the background noise when the plasma density was low was also 5 ns. For a given delay, images were re-acquired 50 times and averaged to account for shot to shot variability in the discharge and to improve the signal-to-noise. The time between physical acquisitions of actual images was 20 s, which is long compared to the characteristic charge relaxation time (ms) which then enables the dielectric array to relax to its pre-breakdown status. Typical current and voltage waveforms for the study are shown in figure 4.

Discharge evolution over a 40 ns interval at atmospheric pressure with quartz media is shown in figure 5 for a 20 kV voltage pulse. (Note that the camera magnification may differ from figure-to-figure, resulting in different apparent sizes of the disks.) The voltage pulse was applied between the anode (pin electrode) on the left-hand side of the image and the planar cathode electrode on the right side. The discharge initiated at the pin anode, where electric field enhancement is high (see figure 3). The discharge then tended to occur in regions of locally enhanced electric field, corresponding to where the dielectric disks are most closely spaced. At $t = 0$ (figure 5(a)), the discharge predominantly forms between the pin electrode and disks 1 and 7. The discharge in this region transitions from a filamentary micro-discharge (FM) to a SIW by 15 ns. The propagation of the SIW leads to discharge formation around disk 6 by 20 ns. The surface wave formation and subsequent propagation is associated with charge deposition by the FM. The deposited surface charge generates an electric component parallel to the surface that supports this propagation mode [18]. In this manner the discharge travels through the media reaching disk 4 about 25 ns later and

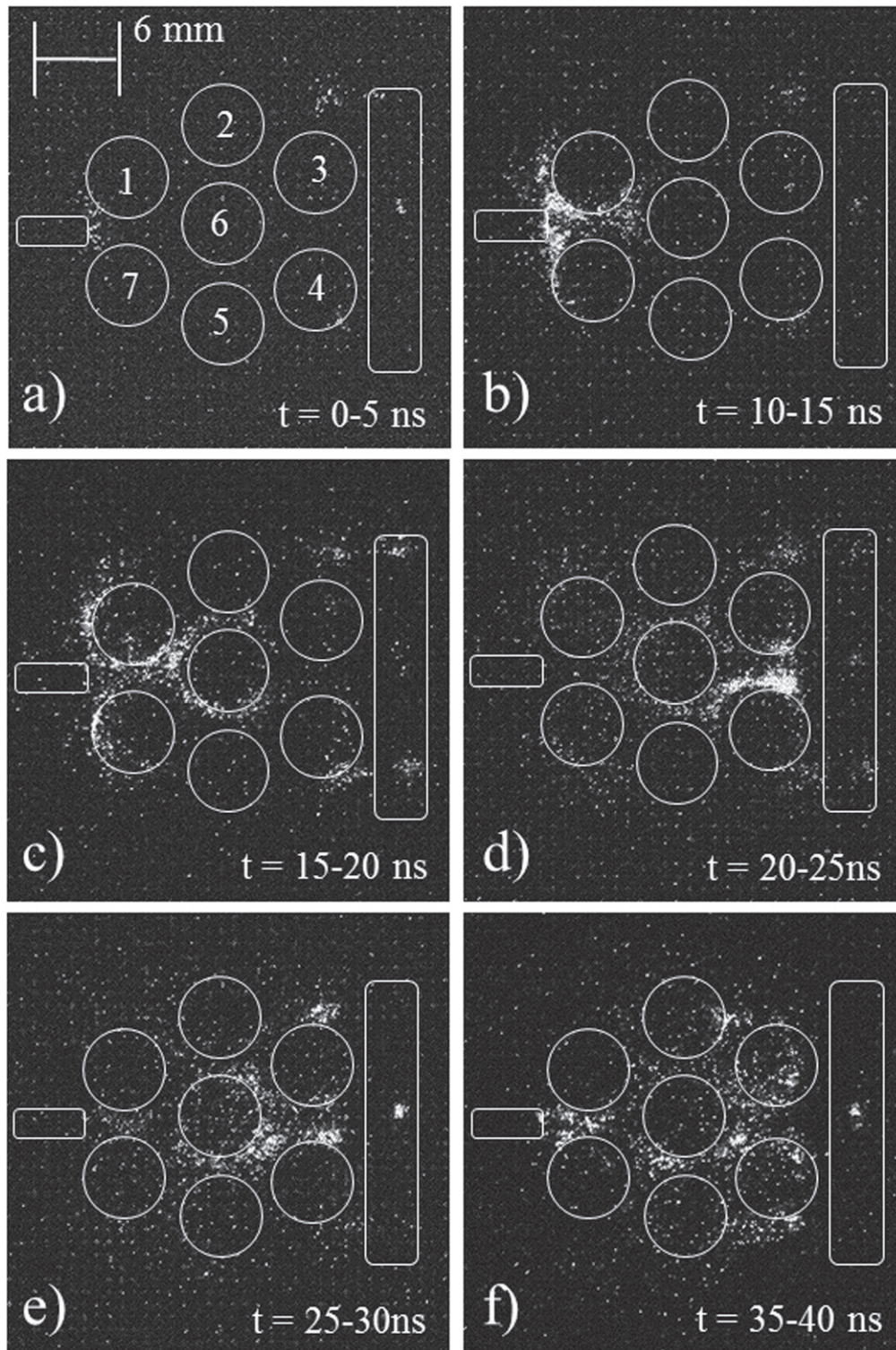


Figure 5. Time-resolved imaging of the 2D-PBR discharge through quartz disks at 1 atm integrated over 5 ns. (a) 0–5 ns, (b), 10–15 ns, (c) 15–20 ns, (d), 20–25 ns. (e) 25–30 ns and (f) 35–40 ns.

finally reaching the cathode by 30 ns. Beyond 30 ns, the discharge re-intensifies in the form of a return stroke which terminates at the pin electrode after 40–45 ns, as indicated by the localized, intense glow there.

To gain insight into the propagation mechanism, a small region between disks including portions of disks 3, 4, and 6 was individually imaged with higher resolution.

These time resolved images are shown in figure 6. The discharge enters the field of view as a SIW at disk 6 in figure 6(a). As this SIW propagates around disk 6, it enters into the region of high electric field between disks 4 and 6, leading to the formation of a micro-discharge between the two disks (figure 6(a)). This micro-discharge and associated charge deposition leads to the formation of a propagating

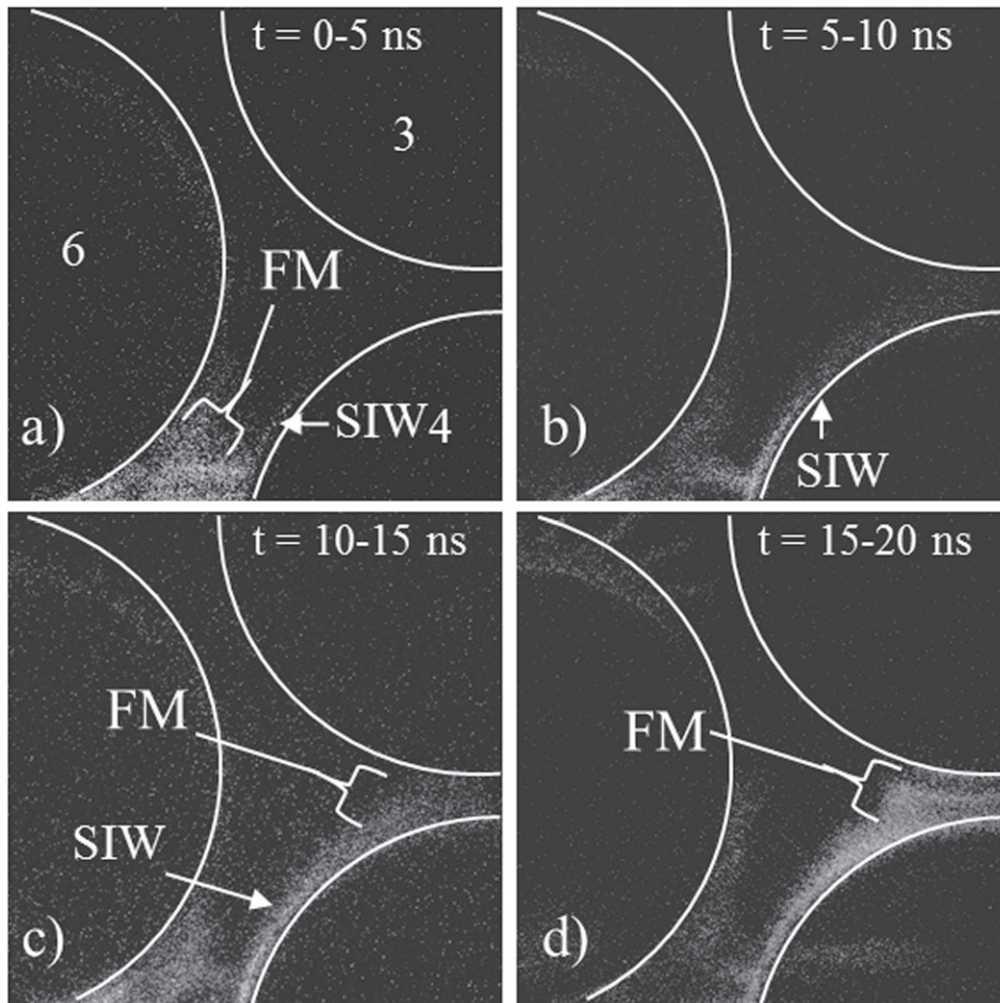


Figure 6. Time-resolved microscopic imaging of the 2D-PBR discharge in the vicinity of quartz disks 3, 4 and 6 at 1 atm integrated over 5 ns. (a) 0–5 ns, (b), 5–10 ns, (c) 10–15 ns, and (d), 15–20 ns.

SIW along disk 4 (figures 6(b) and (c)). Again, as this surface wave enters the region of enhanced electric field between disks 4 and 3 (see figure 3), a FM forms between the disks (figures 6(c) and (d)). The surface discharges tend to translate along the surface of the disks in the general direction of the applied electric field.

Time resolved imaging of discharges through zirconia disks ($\epsilon_r = 26.6$) was also conducted. Imaging of the entire array is shown in figure 7. The mode of propagation, at first, appears to be quite different compared to propagation through the quartz disks. In the quartz array, the discharge tended to propagate through the media as an ionization wave. A FM led to formation and propagation of a SIW propagation which then seeded a FM when the SIW reached the high electric field region in the next gap. With zirconia disks, it was more difficult to discern a clear discharge propagation pattern using the macroscopic lens. With a wider angle perspective, the discharges appeared to be highly localized, occurring largely in regions of high electric field, which is typically largest between adjacent disks.

At early times in the zirconia array, a localized discharge occurred between the pin electrode and disks 1 and 7 (0–5 ns, figure 7(a)), followed by localized discharges near the ground

electrodes (5–10 ns, figures 7(b) and (c)). These discharges are intense, and concentrated at the poles of the disks where the electric field is the largest. These micro-discharges last for 15–20 ns before charging of the dielectrics reduce the electric field in the gap—akin to a DBD. At later times, FMs appear throughout the media aligned with regions of intense electric field (figures 7(c)–(f)). These discharges decay over 10 s of ns, again likely due to charge deposition on the adjacent surfaces, which locally reduces the electric field. Indeed, by 35 ns, all discharges decay away only to reappear near the cathode around 40 ns (figures 7(e) and (f)).

The volume bounded by the surface of three zirconia disks (3, 4 and 6) was imaged with higher resolution, as shown in figure 8. At early times, 0–10 ns (figures 8(a) and (b)), intense localized FM develop in the gaps between adjacent dielectric surfaces. The micro-discharges that bridge the gap between dielectrics gives rise to the formation of weak emission attributed to surface discharges on disks 4 and 3 at $t \approx 15$ –25 ns (figures 8(c) and (d)) in the general direction of the applied electric field. From this perspective, the modes of propagation through the zirconia array were similar to those of the quartz array, with FMs forming SIWs that

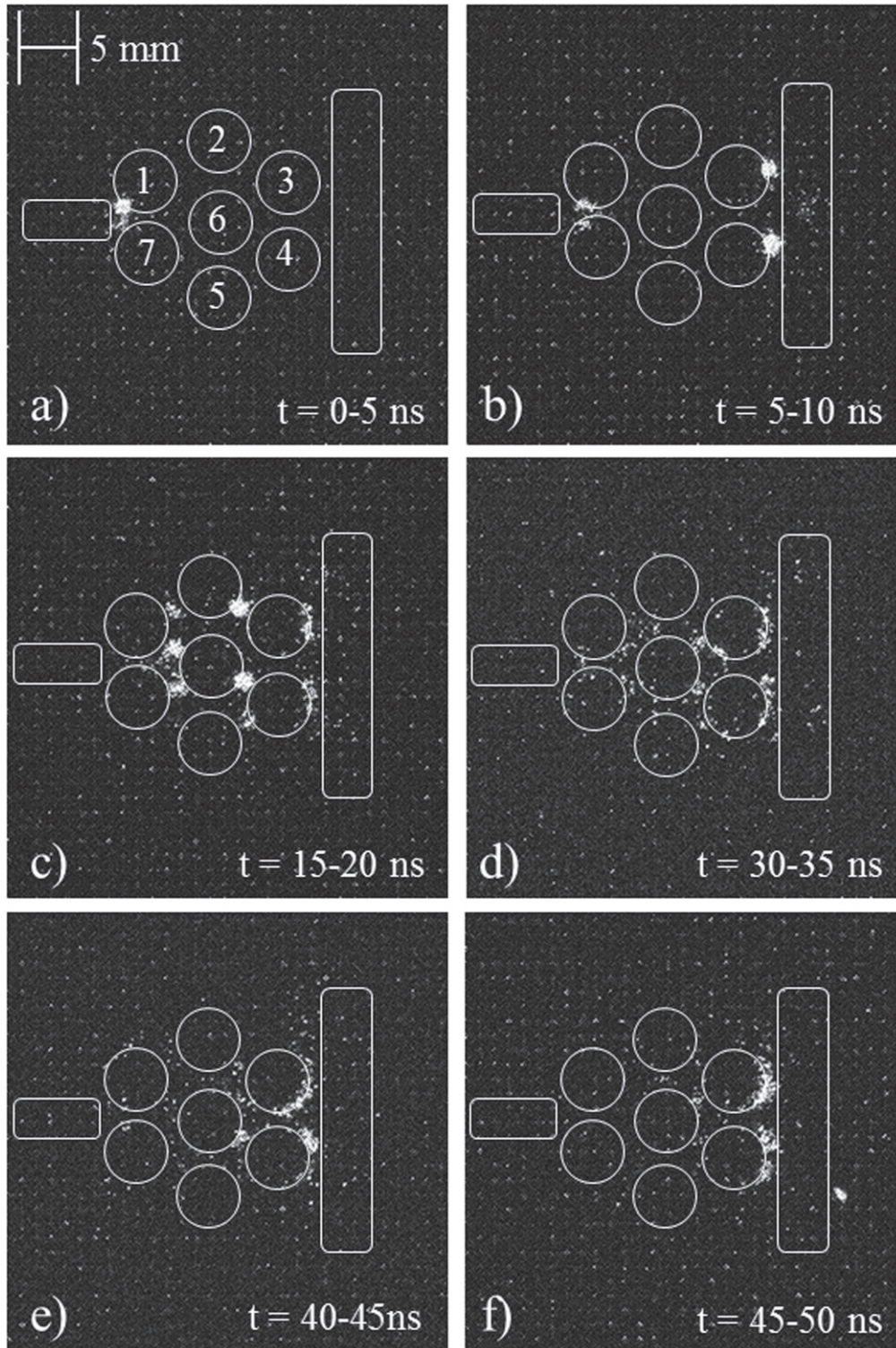


Figure 7. Time-resolved imaging of the 2D-PBR discharge through zirconia disks at 1 atm integrated over 5 ns. (a) 0–5 ns, (b), 10–15 ns, (c) 15–20 ns, (d), 30–35 ns. (e) 40–45 ns and (f) 45–50 ns.

eventually lead back to FMs. This sequence cascades through the array until the grounded electrode is reached. However, the relative intensities of the two modes favor the FM. When using the macroscopic lens (images in figure 7), the contrast between the FMs and SIWs only enabled imaging of the FMs. Both structures were able to be imaged using the microscopic lens.

Based on ICCD light intensity counts, image contrast, and the magnitude of the current spikes (4 times greater for zirconia), the micro-discharges imaged for the higher dielectric-constant zirconia were nearly an order of magnitude brighter than for quartz. Once the discharge develops, charging of the adjacent surfaces will eventually extinguish the micro-discharge across the gap due to the reduction in electric

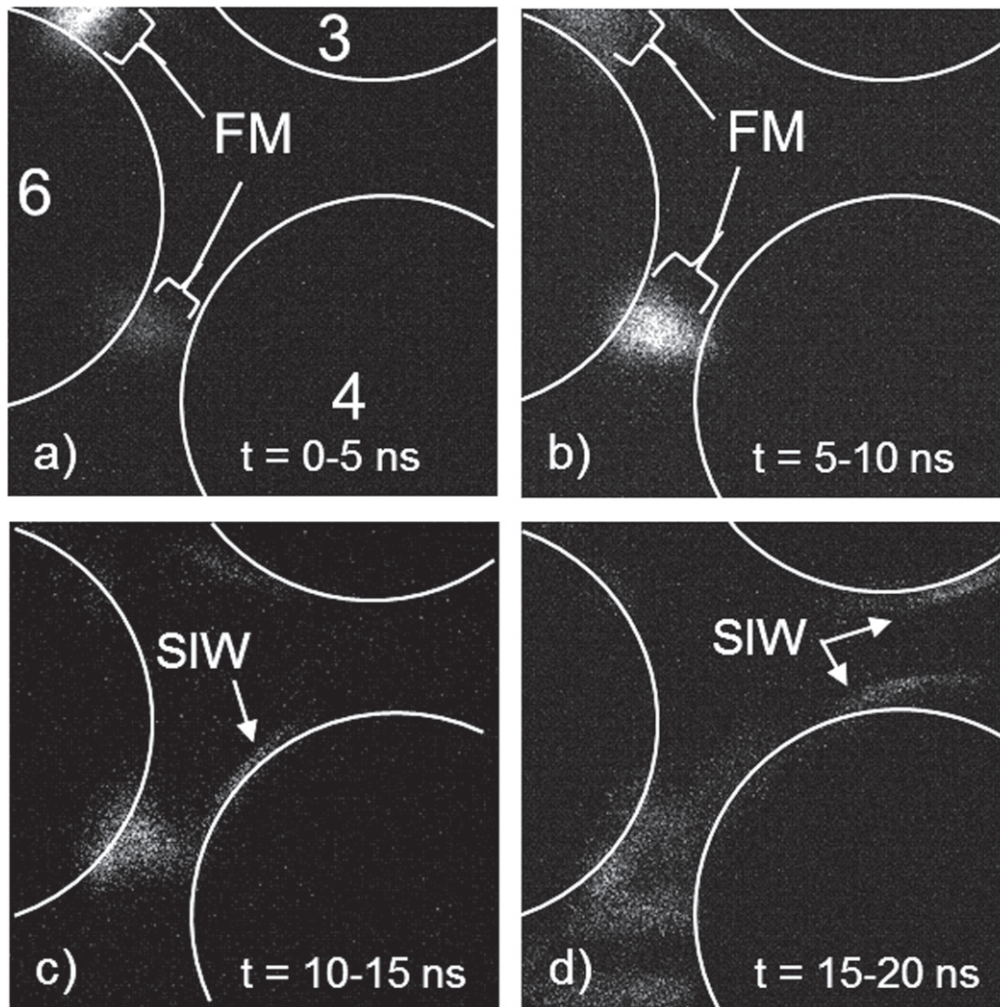


Figure 8. Time-resolved microscopic imaging of the 2D-PBR discharge in the vicinity of zirconia disks 3, 4 and 6 at 1 atm integrated over 5 ns. (a) 0–5 ns, (b) 5–10 ns, (c) 10–15 ns, and (d), 15–20 ns.

field enhancement. It is not clear why the more intense micro-discharges do not seed equally intense surface discharges in zirconia. It is possible that the intense FM collapses the applied electric field locally owing to higher charge deposition, and that this lower electric field is below the threshold to support intense SIWs.

The propagation speeds of the SIWs were calculated using image analysis software to determine the displacement of the SIW over the 5 ns time step. The propagation speed of the SIWs along the surface of the quartz disks was $\approx 3 \times 10^7$ and $\approx 4 \times 10^7$ cm s⁻¹ for the zirconia disks. These values correspond well with those reported by Kang *et al* with an average velocity of 2.5×10^7 cm s⁻¹ and Wang *et al* with 2×10^7 cm s⁻¹ [16, 17]. For example, Petrishev *et al* investigated formation of SIWs on a quartz plate using a high voltage, nanosecond pulse and measured propagation speeds of 5×10^7 cm s⁻¹ [11]. These speeds are commensurate with gas phase streamer propagation speeds. The speeds of the SIWs that do form in zirconia are slightly higher than in quartz, likely due to the higher current and so space charge. The streamer speed tends to increase with increasing space charge derived electric field at the streamer head [24].

A comparison of experimental and modeling results is shown in figure 9. The top row of frames are experimental ICCD images of optical emission between zirconia disks (3, 4 and 6) with an exposure time of 5 ns. The exposures of the images were digitally enhanced to show the features of interest so intensity cannot be directly compared frame-to-frame. The computed results are the densities of the main photo-emissive species in the model ($(N_2(b^1\Pi))$ and $N_2(b^1\Sigma))$). The choice of frames was made to show correlating phenomena. The difference in time scale may be attributed to the 3D effects of electric field enhancement at sharp edges that are not captured in the 2D model. Intense filamentary micro-discharge structures initially form between disks 6 and 3, and disks 6 and 4, as shown in figures 9(a) and (b) (experiment and model). The electrons incident onto disks 3 and 4 charge the surfaces of the dielectrics and SIWs begin forming (figures 9(c) and (d)). As the potential between the disks drops due surface charging, the intensity of the FMs decreases, and the propagating SIWs become the brightest regions in the images (figures 9(e)–(h)). The SIWs are cathode-seeking discharges—regardless of the polarity of the applied voltage, as mentioned in our previous work [18]. This

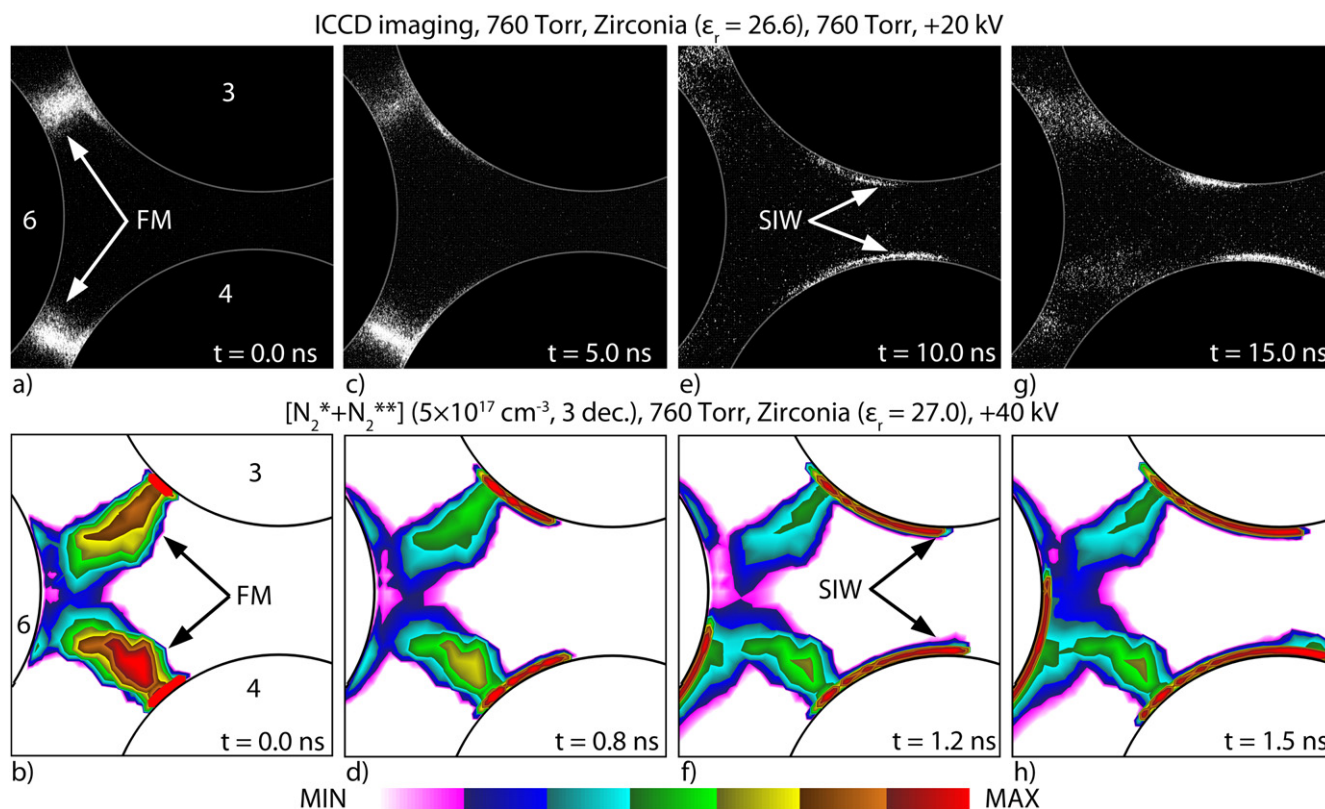


Figure 9. Transition from micro-discharges to surface ionization waves between disks 3, 4, and 6 and at sequential times. (Top) experimental ICCD imaging and (bottom) computed densities of light-emitting species from the model (bottom). The disparity in time between the model and the experiment arises from the different voltages being applied.

trend results from electrons impacting the dielectric surfaces leaving behind a region of positive space charge in the gas-phase. Through a process that is similar to that of the propagation of positive streamers, the positive SIWs then propagate down the potential gradient.

The discharges just discussed were sustained with a voltage pulse amplitude of 20 kV. Investigations were also performed for atmospheric pressure discharges through zirconia disks for voltage amplitudes of 16, 17, 19, and 20 kV, as shown in figure 10. The corresponding discharge power levels were as follows: zirconia (20–16 kV): 5.6, 5, 3.9, 3.5, and 2.8 mJ, respectively and quartz (20–16 kV) 5.3, 4.8, 4.0, 3.7, and 3.2 mJ. The trends for discharge formation and propagation were basically the same as a function of voltage over this range, with the intensity and speed of discharge formation increasing with increasing voltage. The contrast of the images for 19 and 20 kV (figures 10(a) and (b)) shows more intense FMs whereas at the lower voltages of 16 and 17 kV (figures 10(c) and (d)) the plasma appears to be more diffuse.

4. Discharge evolution as a function of pressure

Discharge formation in PBRs at 1 atm is typically highly localized, propagating through the medium essentially as a sequence of ionization waves within gaps (FM) or along surfaces (SIW). The dominance of these structures is in part

due to the high pressure for which electron energy transport is dominated by local phenomena. As pressure decreases and electron energy transport becomes less local, we expect systematic differences from discharge propagation at 1 atm. To investigate these trends, imaging of discharges in the 2D-PBR was performed at reduced pressure. Beyond understanding propagation mechanisms, there may be a practical basis for operating at reduced pressure as well. Although most chemical processing using PBRs is performed at atmospheric pressure to minimize the costs of managing pumping and vacuum, it is not clear that atmospheric pressure is optimum in terms of discharge propagation, filling the volume of the PBR and utilizing all of the catalyst. As the pressure is reduced for a given applied voltage, E/N will increase which would produce more energetic electrons. Reduced pressure and reduced collisionality that might otherwise confine SIW to close proximity of surfaces would also tend to increase the volume of the plasma.

During sub-atmospheric pressure experiments, the peak voltage was kept constant at 12 kV with a 120 ns pulse width. Experiments were performed at 200, 100, 50 and 10 Torr. Discharge images could not be captured above a few hundred Torr due to the inability to initiate a breakdown through the quartz disks at 12 kV.

Images of the time evolution of the discharge with quartz disks in the entire array at 100 and 50 Torr are in figures 11 and 12, respectively. In general, when reducing pressure, local emission intensity decreases. In both lower pressure

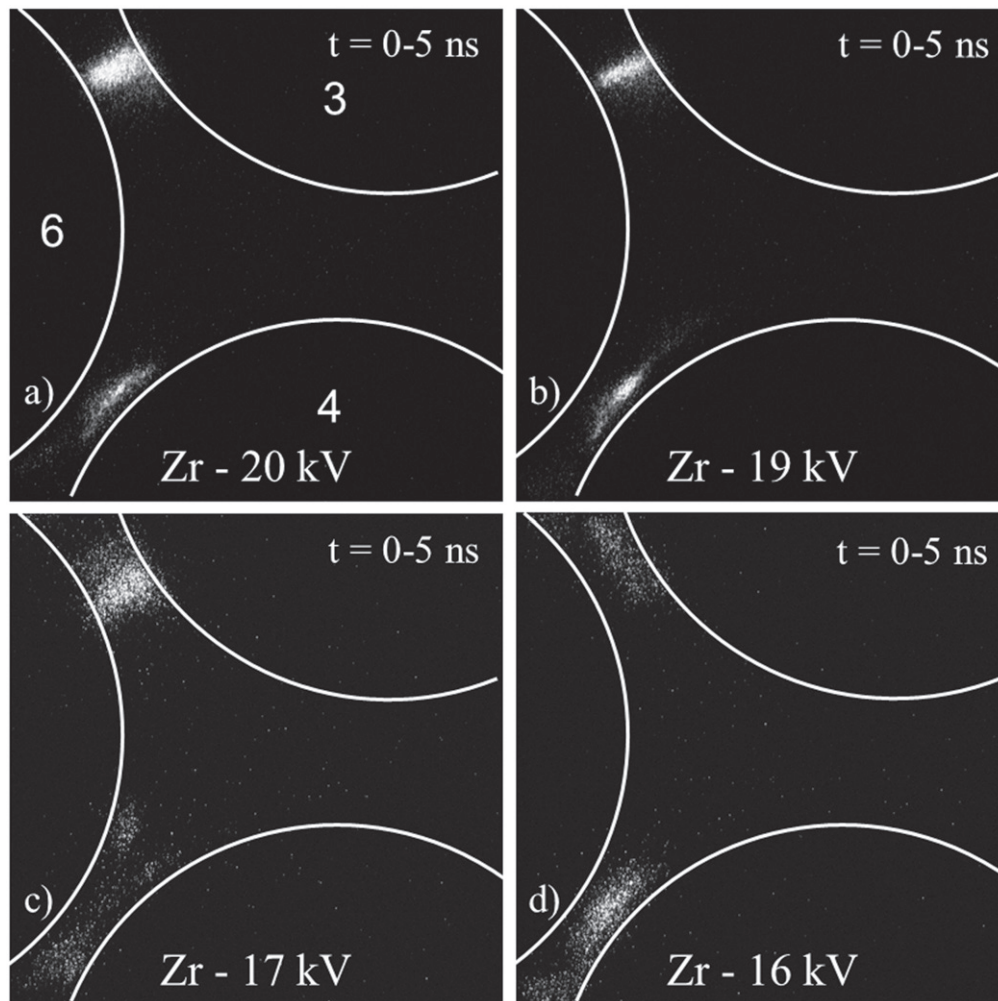


Figure 10. Imaging of emission of discharges through zirconia disks (5 ns exposure) at atmospheric pressure. (a) 20 kV, (b) 19 kV, (c) 17 kV and, (d) 16 kV.

cases, the discharge appears to translate through the array as a SIW with the thickness of plasma extending well into the gap between disks. Some of this extension into the voids might possibly be due to sheath expansion at the lower pressures. The discharge becomes less surface-hugging and bends away from the surface, likely due to the higher mobility of charges being able to more rapidly charge the surface at lower pressures. As the pressure is further reduced to 10 Torr, shown in figure 13, SIWs propagating on adjacent surfaces merge in the volume between the dielectric disks. In spite of operating at higher values of E/N than the discharges at 1 atm, the images do not indicate that FM form in the gaps between disks where the E/N is largest. This is likely due to the intensity of the SIWs saturating the response of the ICCD.

To more closely investigate the formation of FMs at low pressure, a mask was placed over the 2D cell. The mask restricted the ICCD to collecting light from the region between disk 6 and 4 where FMs were expected to form. The resulting images are in figure 14. The right side of the figure has images taken with the mask in place. The left side of the figure has images taken at the same voltage and exposure time but without the mask. Even at a pressure of 50 Torr, FMs form in the high

E/N gaps, and transition to an SIW on the adjacent disk. The angle of the FM, however, is not strictly perpendicular to the surfaces at low pressure. This is due to the higher E/N throughout the cell at low pressure. For example, at 1 atm the vacuum value of E/N at the center of the void between disks 1, 7 and 6 is 25 Td, which is not high enough to self-sustain a discharge in air. ($1 \text{ Td} = 10^{-17} \text{ V cm}^2$.) At 50 Torr, the E/N in the void is 220 Td, which exceeds the threshold for sustaining a discharge in air. At lower pressure, propagation appears to be more influenced by the applied axial electric field than the electric field enhancement that occurs in the gaps between disks (or due to the polarization of the disks at their poles).

In the gaps between disks 6 and 3, and between 6 and 4, locations where FM occur perpendicular to the surfaces at 1 atm, the discharge propagates parallel to the surfaces at low pressure. In fact the discharge propagates from the top and bottom of disk 6 leaves a void where natural electric field enhancement occurs by polarization of the disks. To investigate this region, a mask was applied which largely blocked emission from the higher intensity FMs and SIWs. The resulting images showed diffuse, volumetric plasma emission throughout the void at low pressures (50–300 Torr).

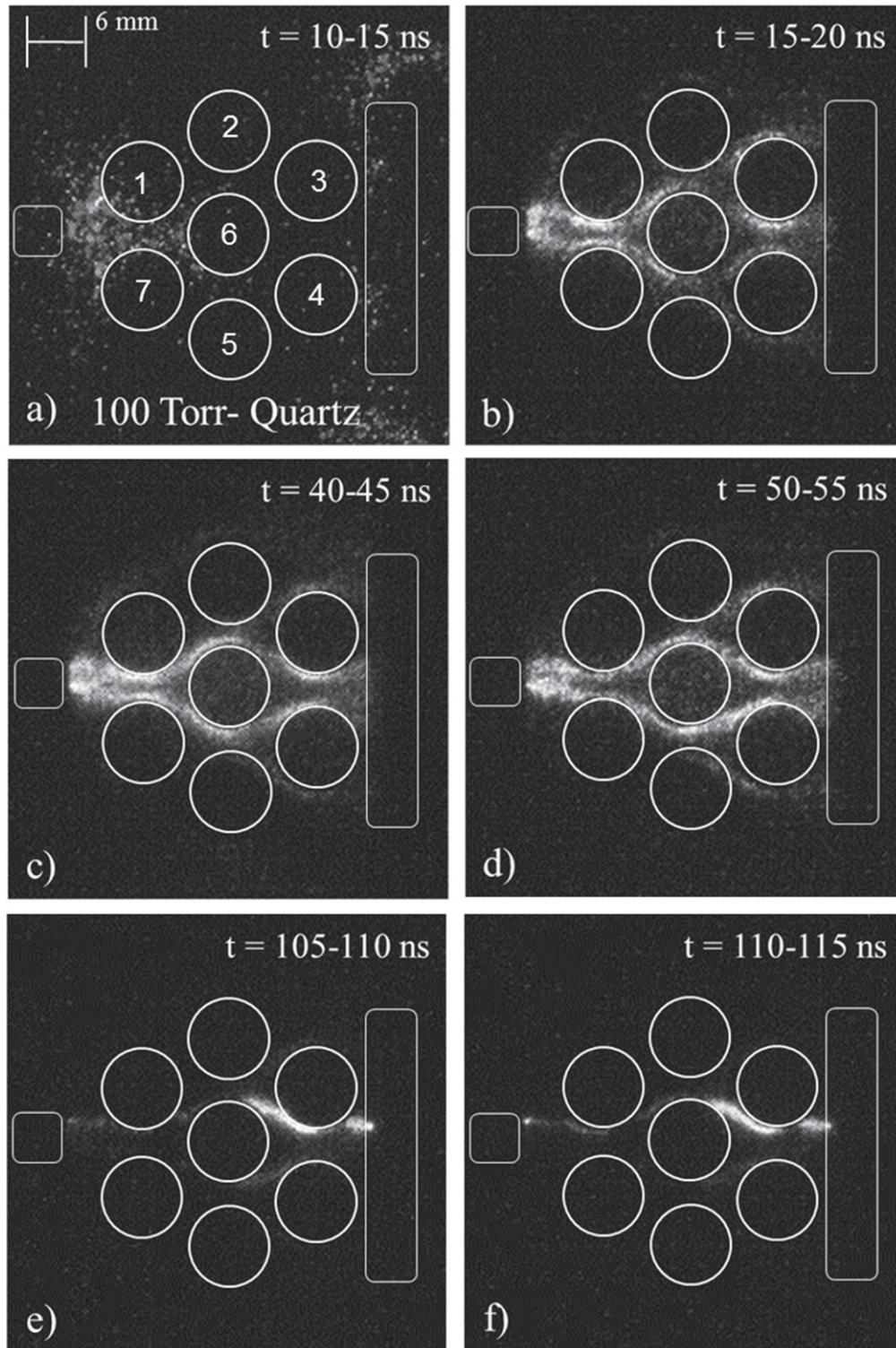


Figure 11. Time-resolved imaging of the 2D-PBR discharge through quartz disks at 100 Torr integrated over 5 ns. (a) 10–15 ns, (b), 15–20 ns, (c) 40–45 ns, (d), 50–55 ns. (e) 105–110 ns and (f) 110–115 ns.

The same procedure was performed at 1 atm and little, if any, plasma emission was observed in the void. Values for α (ionization coefficient), and η (attachment coefficient) were computed from the results of *nonPDPSIM* in the void between the disks 3, 4, and 6. As the pressure increases, α decreases from 9.74 cm^{-1} at 50 Torr to 0.21 cm^{-1} at 200 Torr

whereas η increases from 0.82 to 2.53 cm^{-1} . These results indicate that the net rate of ionization, $\alpha - \eta$, transitions from being positive (net ionization) in the void to negative (net attaching) between 100 and 200 Torr. The trends in net ionization predicted by the model correlate well with the experimentally observed change in the mode of propagation.

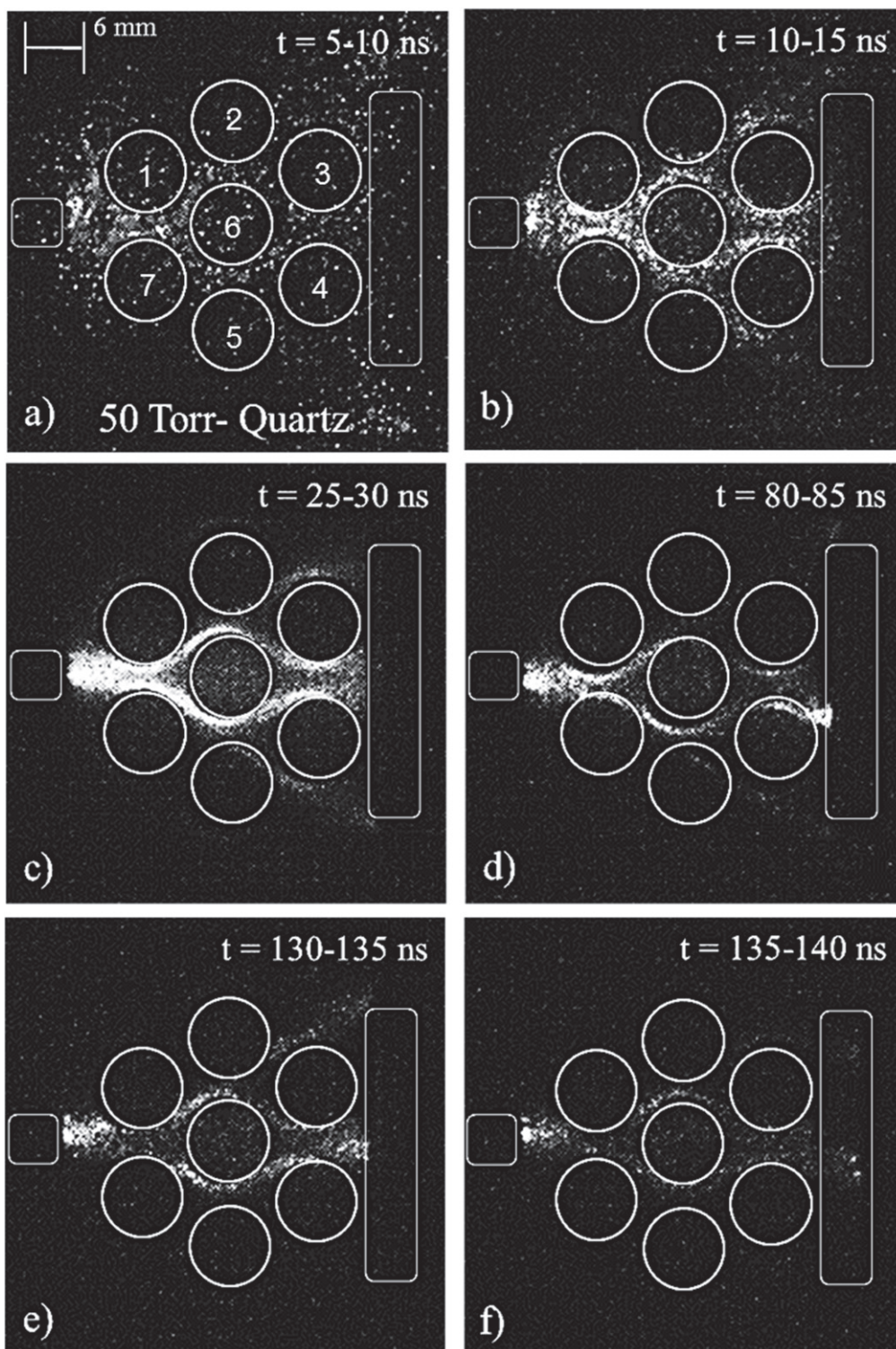


Figure 12. Time-resolved imaging of the 2D-PBR discharge through quartz disks at 50 Torr integrated over 5 ns. (a) 5–10 ns, (b), 10–15 ns, (c) 25–30 ns, (d), 80–85 ns. (e) 130–135 ns and (f) 135–140 ns.

With higher α , plasma propagation occurs in the void, however as the system becomes net attaching, plasma production in the void diminishes.

Time resolved images of discharge development with zirconia disks at 50 Torr are shown in figure 15. Discharge development is similar to that in the quartz array, albeit with

higher emission intensity. The discharge slowly develops between 5 and 10 ns, after which the array quickly fills with a highly developed discharge. Here again, a surface wave like discharge propagates through the array with the interstitial spaces being filled with higher density plasma than the seemingly empty voids. The discharge appears to cover the

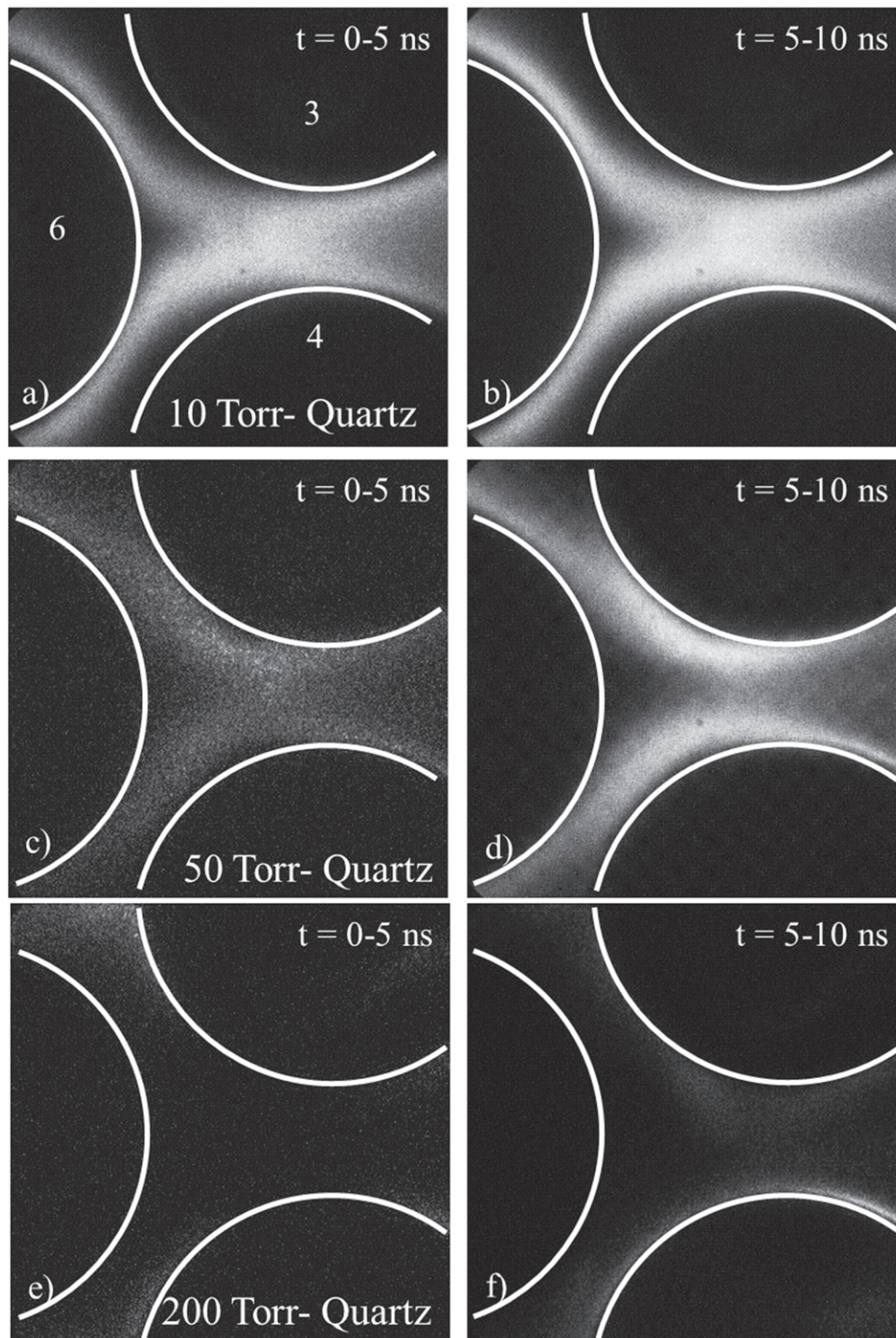


Figure 13. Time-resolved imaging of the 2D-PBR discharge through quartz disks for 10, 50, and 200 Torr integrated over 5 ns. (a) 10 Torr, 0–5 ns; (b), 10 Torr, 5–10 ns; (c) 50 Torr, 0–5 ns; (d), 50 Torr, 5–10 ns; (e) 200 Torr, 0–5 ns; (f) 200 Torr, 5–10 ns.

zirconia disks more extensively than the quartz disks. The time resolved images of discharge propagation through zirconia disks in the vicinity of disks 3, 4 and 6 are shown in figure 16 for pressures of 10 Torr through 200 Torr. With the larger permittivity of zirconia, the discharge behavior that occurs at 1 atm is recovered by 200 Torr. At 10 Torr, the discharge is dominated by SIWs. At 200 Torr, FM are

produced in the gaps, followed by the launch of SIWs, as at 1 atm.

The transition between SIW to FM discharges in the zirconia array occurs near 200 Torr. This transition is shown by the images in figure 17 for pressures between 180 and 210 Torr. At 180 Torr, the applied E/N is large enough that the discharge occurs in regions outside the field-intensified

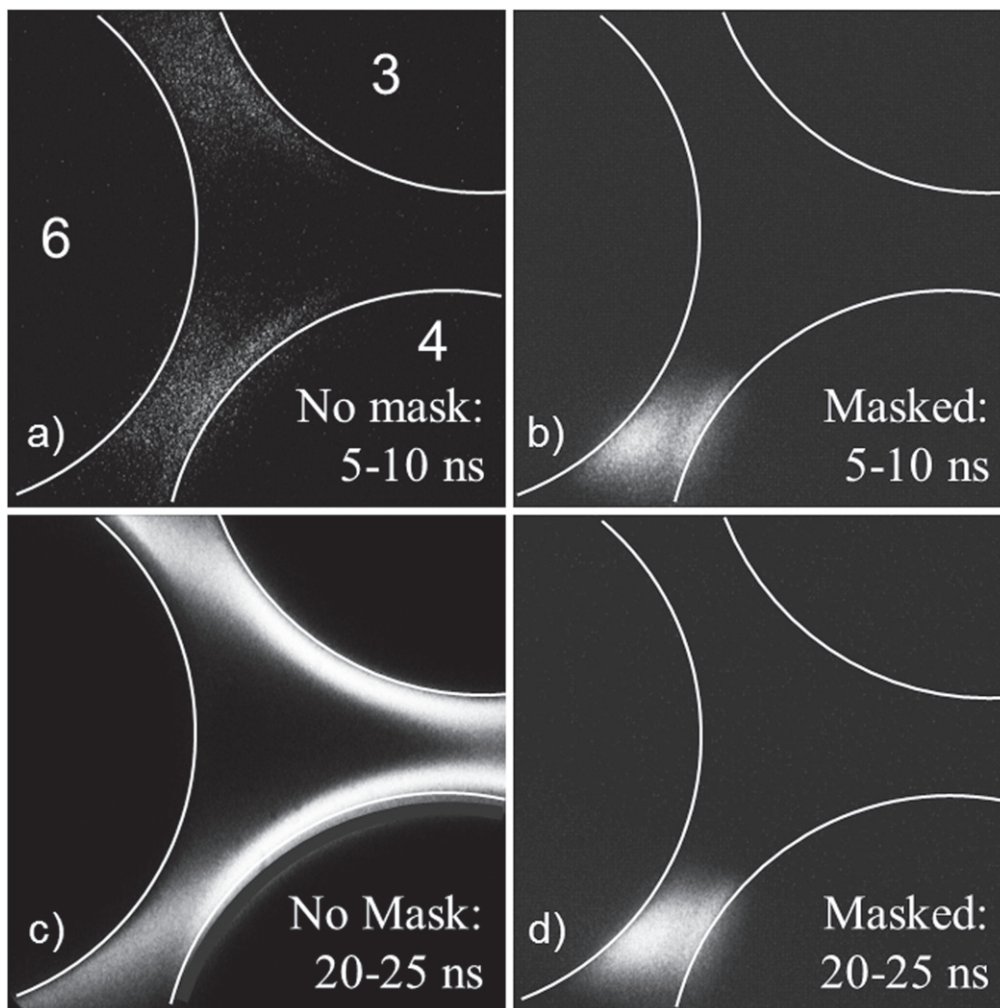


Figure 14. Imaging of discharges through zirconia disks at 50 Torr (5 ns exposure) with and without masking. The masking blocked emission from the surface ionization waves. (a) Without mask, 5–10 ns, (b) with mask, 5–10 ns, (c) without mask, 20–25 ns and (d) with mask 20–25 ns.

gaps. As the pressure increases from 190 to 200 Torr, the E/N outside the gaps decreases below self-sustaining, leaving the gaps having large enough E/N to initiate the discharge in the form of FM.

The thickness of the SIW was measured from the ICCD images and is shown in figure 18. The measurement was made from the surface of the disk to the edge of the luminous region and did not consider possible sheath effects that may elevate the luminous region above the disk. The SIW thickness varied inversely with the pressure, suggesting that the thickness is limited by the electron–neutral mean free path. The surface wave thickness varied linearly with mean free path regardless of type of material, though SIW thickness tended to be greater for the quartz disks. This trend is consistent with the ICCD images being more intense for the zirconia, implying higher plasma density, smaller Debye length and so thinner SIW thickness. Time integrated images over 1 ms were recorded for pressures of 10–200 Torr, and are shown in figure 19 for the zirconia disks. These images demonstrate that in general, the discharge volume increases with decreasing pressure.

5. Modeling of propagation through quartz and zirconia arrays

The geometry used for the simulations is a good-faith reproduction of the experiment and is shown in figure 20. The numerical mesh uses 12 746 nodes, with a resolution varying from 0.14 cm to 30 μm . Seven dielectric disks with diameters of 1.8 mm and separation distance of 700 μm were placed between the electrodes in a symmetric pattern. The size of the disks was maintained to be consistent with our previous work [18]. While the disks are smaller than those used in the experiments, these differences only impact quantitative values, and not the trends or conclusions in this work. The geometry has a depth of 0.5 cm to allow for volumetric calculations. The gas is humid air ($\text{N}_2/\text{O}_2/\text{H}_2\text{O} = 78/21/1$) at the initial temperature of 300 K. Pressures of 760, 200, 100, and 50 Torr were simulated with a positive potential applied to the top electrode, while the bottom electrode was grounded. The anode in the numerical mesh was rounder than in the experiment to avoid numerical issues resulting from too-steep an electric field gradient. The applied voltages were +40 kV

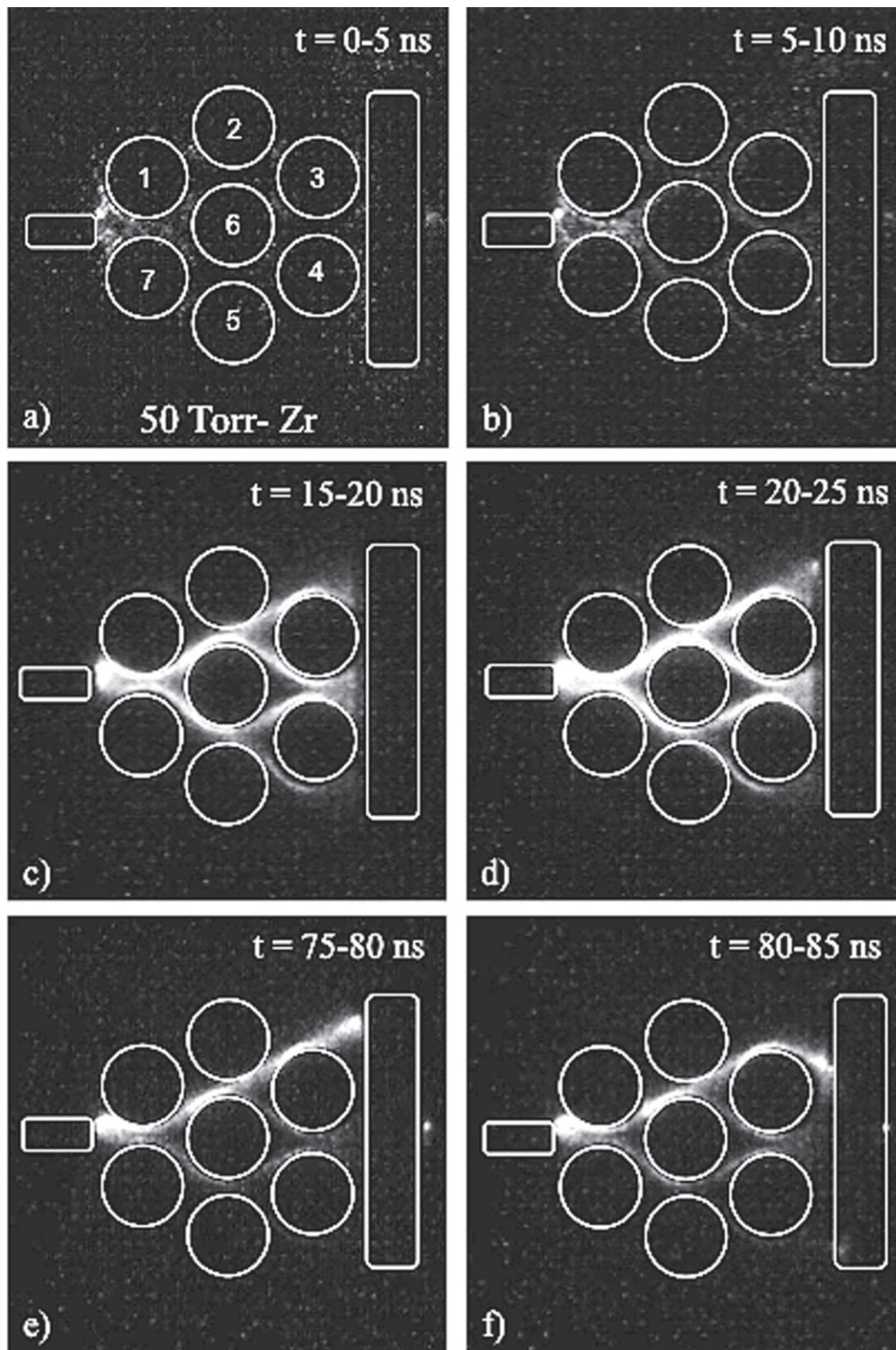


Figure 15. Time-resolved imaging of the 2D-PBR discharge through zirconia disks at 50 Torr integrated over 5 ns. (a) 0–5 ns, (b), 5–10 ns, (c) 15–20 ns, (d), 20–25 ns. (e) 75–80 ns and (f) 80–85 ns.

for the 760 Torr cases, and +24 kV for the low-pressures. These values of potential are double that of the experimental voltages to account for the three-dimensional effects of electric field enhancement at sharp edges of electrodes that are not captured in the 2D model. The outcome is that phenomena occur more rapidly in the model while capturing the experimental trends. The gas was uniformly pre-ionized to an

electron density of $1 \times 10^6 \text{ cm}^{-3}$ (balanced by O_2^+ and N_2^+) at 760 Torr. The magnitude of the pre-ionization was then scaled down for the low-pressure cases to maintain a constant pre-ionization fraction. A plasma seed with a diameter of 0.05 cm and peak density of 10^{12} cm^{-3} was also placed at the tip of the top electrode to provide a consistent starting location of the positive streamers.

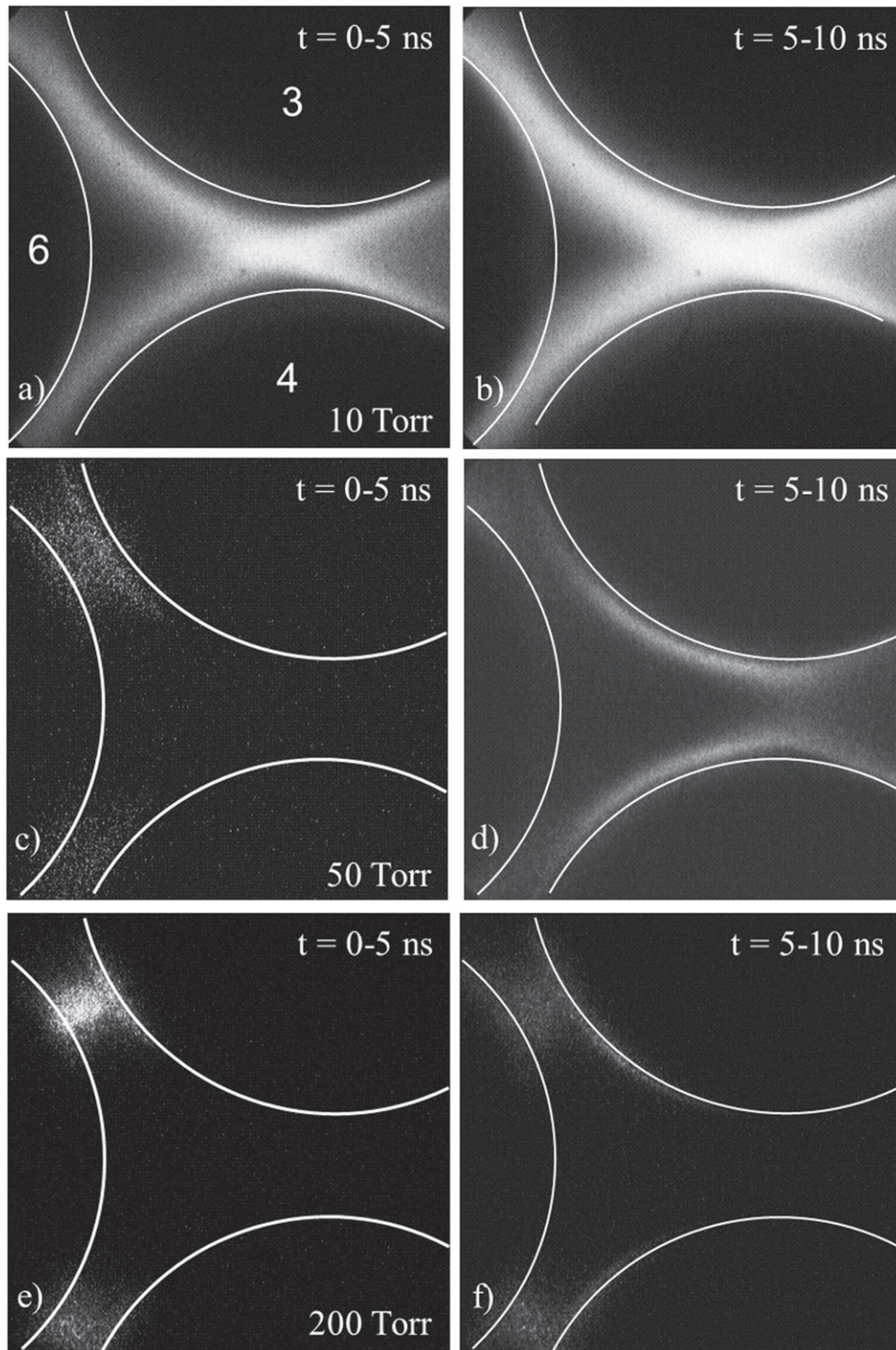


Figure 16. Images of the 2D-PBR discharge through zirconia disks for 10, 50, and 200 Torr integrated over 5 ns. (a) 10 Torr, 0–5 ns, (b) 10 Torr, 5–10 ns, (c) 50 Torr, 0–5 ns, (d) 50 Torr, 5–10 ns, (e) 200 Torr, 0–5 ns, (f) 200 Torr, 5–10 ns.

The base case is a discharge at atmospheric pressure with dielectric disks having the approximate permittivity of quartz, $\epsilon_r = 4.0$. This is slightly higher than the experimentally measured value, but not significant enough to impact the results. The resulting discharge evolution is shown in figure 21. With application of voltage to the top electrode, the plasma seed avalanches and propagates from the tip similarly

to a positive streamer, depending on photoionization seeding electrons in front of the streamer head. The electrons are then accelerated towards the positive space charge in the head of the streamer, leaving behind positive ions which then become the new streamer head. The electron density in the initial streamer (figure 21(a)) peaks at $\approx 6 \times 10^{14} \text{ cm}^{-3}$ while the photoionization source term near the head of the streamer is

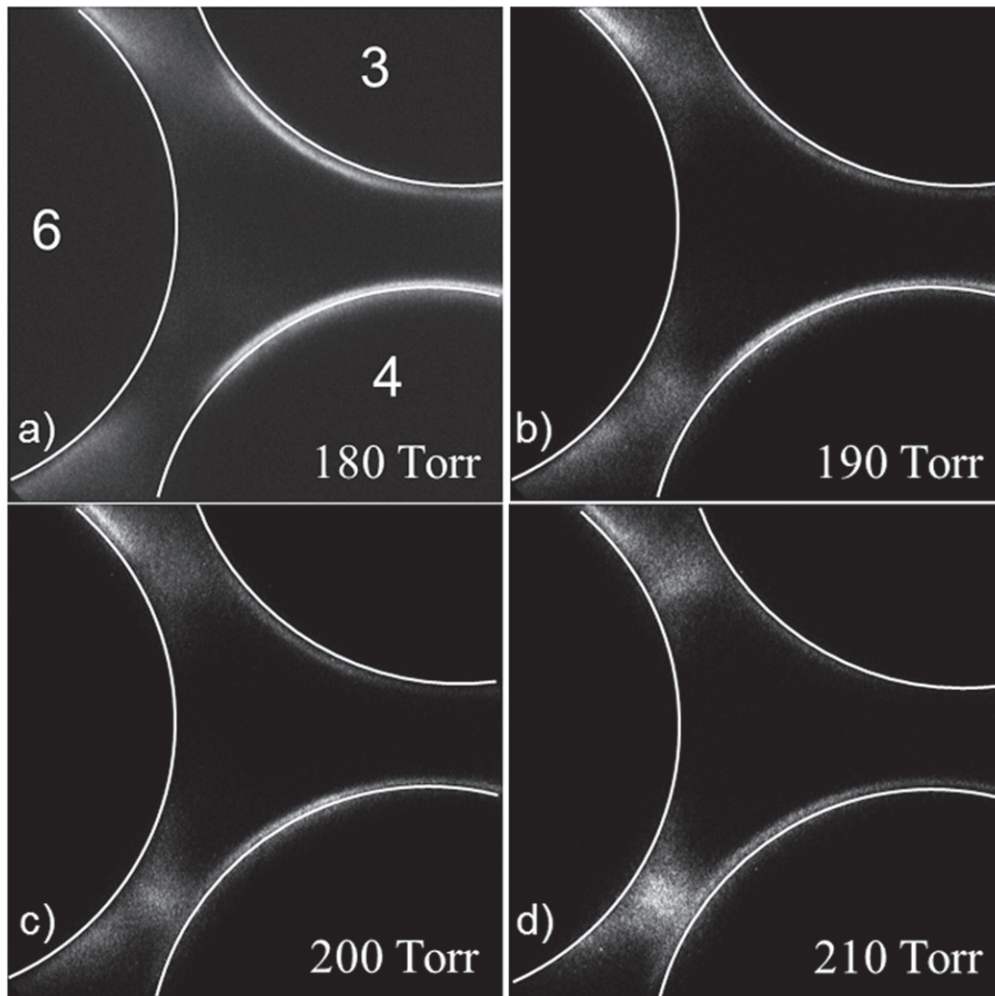


Figure 17. Images (10 ns exposure) capturing the transition from SIW, volumetric discharges to micro-discharges with increasing pressure. (a) 180 Torr, (b) 190 Torr, (c) 200 Torr and (d) 210 Torr.

$1.2 \times 10^{16} \text{ cm}^{-3} \text{ s}^{-1}$. At this time, the streamer continues to propagate downwards in the direction of the ground electrode.

Owing to its high conductivity, as the plasma expands through the array of disks, the size of the spatial region over which the applied voltage drops decreases with time. This results in an increase in the peak E/N between the disks. The E/N between the bottom-most disks and the grounded electrode then increases from $\approx 350 \text{ Td}$ to $\approx 500 \text{ Td}$ in figure 21(b). In the gap between disks (disks 1 and 5; 7 and 2) there is an increase in E/N from $\approx 290 \text{ Td}$ to $\approx 470 \text{ Td}$. These electric fields are strong enough to allow for formation of discharges in between the disks themselves (figures 21(b)–(d)). Similar processes then occur between the middle and bottom row of disks (figures 21(c) and (d)). The discharges initially take the form of positive streamers propagating through the gaps. Once the gaps are bridged, stable micro-discharges form. This mechanism of plasma formation is the same as that in negative discharges described in our previous work [18]. In both cases, the electric field enhancement due to the dielectric disks produces formation of positive, cathode-directed streamers (or re-strikes), which are the seed for the formation of micro-discharges.

The electron densities in the micro-discharges are maximum near the surfaces, and have peak values approaching

$\approx 6 \times 10^{15} \text{ cm}^{-3}$. The discharge column of the micro-discharges are relatively neutral, with space-charge values in the center of the column of $\approx +3.5 \times 10^{-9} \text{ C cm}^{-3}$ (ion excess of $2 \times 10^{10} \text{ cm}^{-3}$, or a fraction of 4×10^{-6}). Simultaneously, the plasma continues to charge the surfaces of the disks, eventually reaching a value of $\approx +4 \times 10^{-6} \text{ C cm}^{-2}$ (2.5×10^{13} charges cm^{-2} or a site occupancy of 2%–3%). This charge deposition produces electric field vectors parallel to the surfaces of the dielectric, which then enables the formation of the SIWs. For example, the electron density, electron temperature, surface charge and electric field are shown in figure 22 on the surface of disk 1. The magnitude of the electric field is shown by the contours while the arrows show the direction of the electric field. As the surface charges and surface-parallel electric field vectors form, electrons accelerate along the dielectric. The surface charge shields the potential at the surface of the dielectric, while the volume charge in the gas-phase produces a peak in the electric field of 200 kV cm^{-1} or $E/N = 820 \text{ Td}$, well in excess of the avalanche value for air. This local maximum results in electron densities of up to $4 \times 10^{16} \text{ cm}^{-3}$. At the head of the SIW propagating in both directions, electric fields in excess of 850 Td produce a local maximum electron temperature of $T_e \approx 9.0 \text{ eV}$.

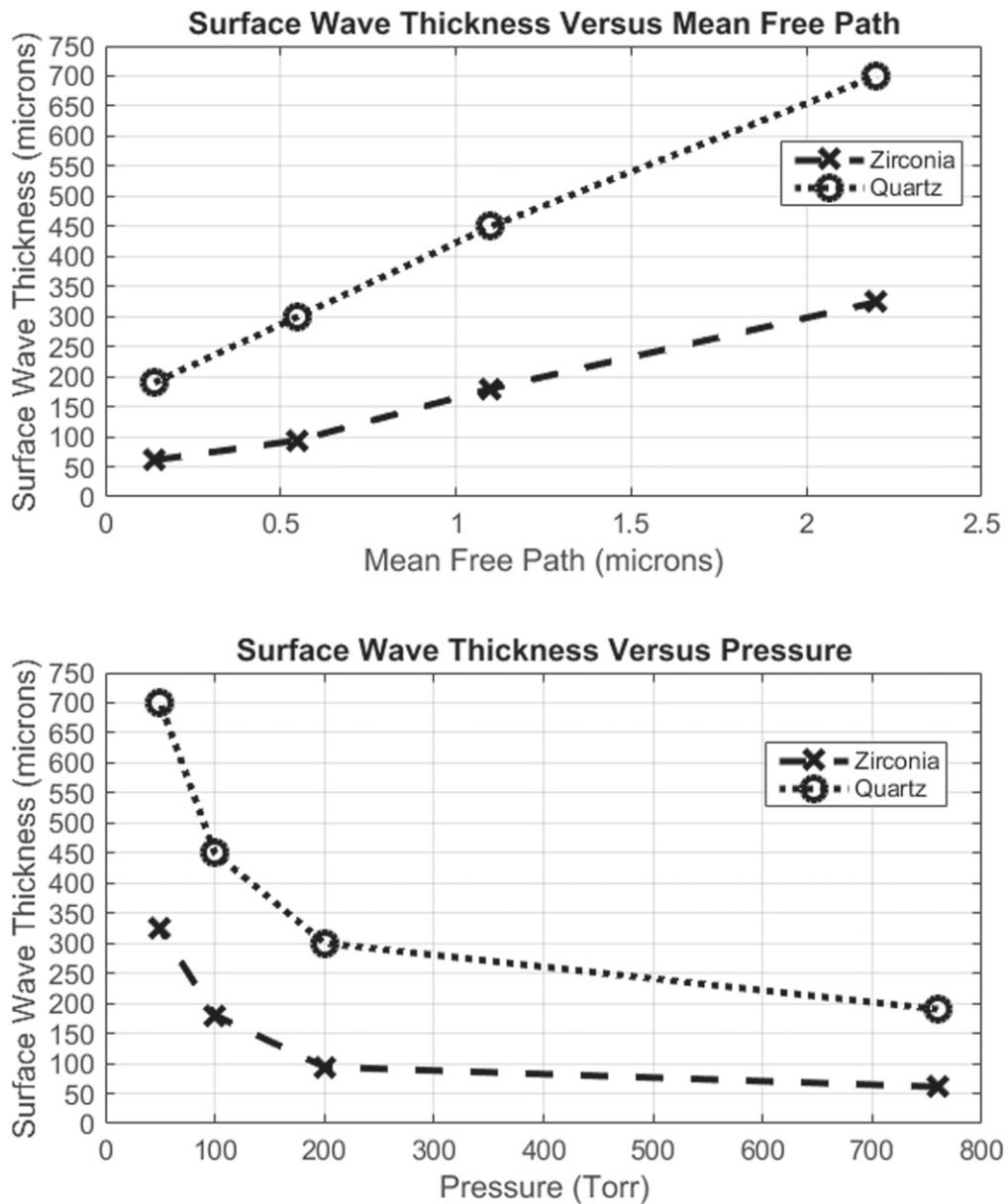


Figure 18. Surface wave properties for zirconia and quartz disks. (a) Surface wave thickness as a function of electron mean free path and (b) surface wave thickness as a function of pressure.

Electron densities in the 2D-PBR for a permittivity of the disks of $\epsilon/\epsilon_0 = 27.0$ corresponding to zirconia are shown in figure 23. The small asymmetry in the electron density is due to high sensitivity of the model to very small differences in the distribution of mesh nodes. Since we do not have explicit control over the meshing algorithm, the mesh between individual disks is not exactly alike, a small degree of asymmetry is expected in the extremely high electric fields that occur in the IW and SIW. As in the experimental results, the computed trends for zirconia are similar to those for quartz. The initial streamer starts at the tip of the electrode and connects with the top-most dielectric disks. Breakdown between the dielectric disks then follows, resulting in formation of FM. The time required for breakdown between all disks decreased from ≈ 8 ns for

quartz disks to ≈ 6 ns due to the increased field enhancement provided by zirconia. The plasma between the bottom-most disks and the grounded electrode forms at an earlier time when compared to quartz. This behavior mirrors the experimental results, and is due to the additional field enhancement resulting from the higher dielectric constant.

The initial ($t = 0$ s) values of E/N in the regions of field enhancement between the higher permittivity disks, from ≈ 290 Td to ≈ 350 Td, are above the avalanche threshold which produces nearly simultaneous breakdown and formation of FM throughout the array. The propagation of the initial ionization wave is therefore obstructed which may explain the change in the mode of propagation that is observed experimentally. The experimental imaging shows that with quartz disks, a sequential breakdown progresses from the anode to

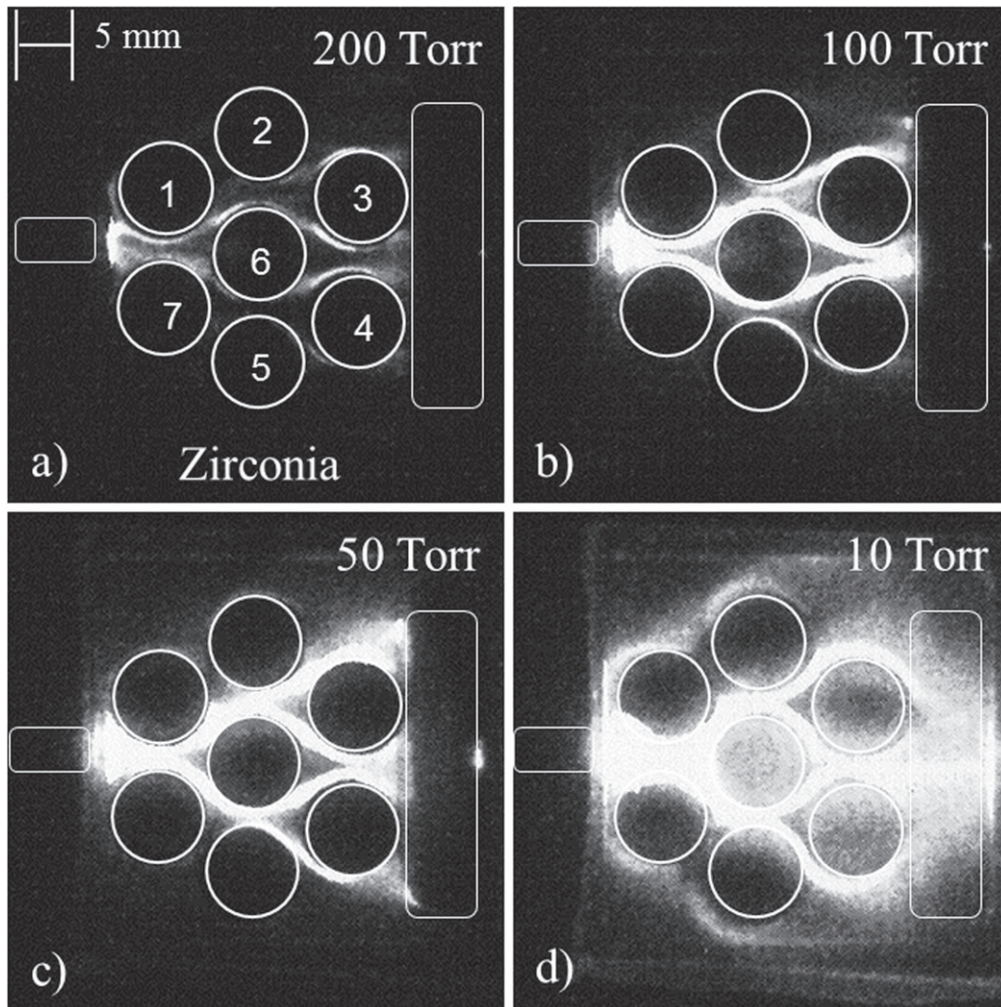


Figure 19. Time-integrated images integrated over 1 ms for discharges through zirconia for different a pressure using the macro lens. (a) 200 Torr, (b) 100 Torr, (c), 50 Torr and (d) 10 Torr.

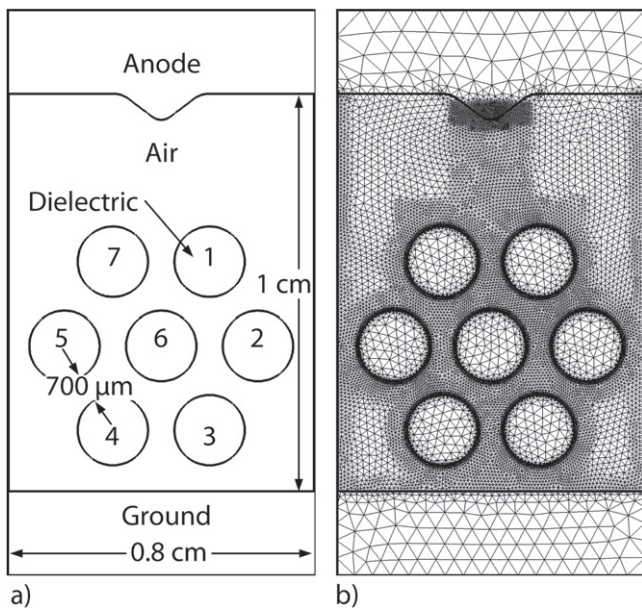


Figure 20. Computational domain. (a) Geometry with disk numbers. (b) Unstructured mesh having 12 746 nodes with spacing between 0.14 cm and 30 μm.

the ground (figure 5). With the zirconia disks (figure 7), a more stochastic behavior took place, with plasma forming randomly in the gaps between disks.

The higher electric field between the individual disks with zirconia leads to formation of higher-density FM. For example, the electron density in the center of the plasma column between disks 6 and 7 increases from $n_e \approx 3.9 \times 10^{14} \text{ cm}^{-3}$ with quartz disks to $n_e \approx 2.2 \times 10^{15} \text{ cm}^{-3}$ with zirconia disks. With the capacitance of a disk being directly proportional to permittivity, a larger amount of charge can be stored on the surfaces of the zirconia disks before the SIWs are launched, which then occurs at a later time compared to quartz allowing for a longer time for the FM to develop. For example, with quartz disks, the surface of disk 7 charged to $1.6 \times 10^{-5} \text{ C cm}^{-2}$ before a SIW began propagating. This value increased to $2.9 \times 10^{-5} \text{ C cm}^{-2}$ with zirconia disks. With the capacitance of the quartz disks being smaller than that of zirconia, the time required to fully charge the quartz surfaces is shorter, which then enables the SIWs to propagate at a higher speed in addition to starting at an earlier time. Since the experimental imaging integrates emission (even over the 5 ns observation window), the surface discharges then appear less intense with quartz disks.

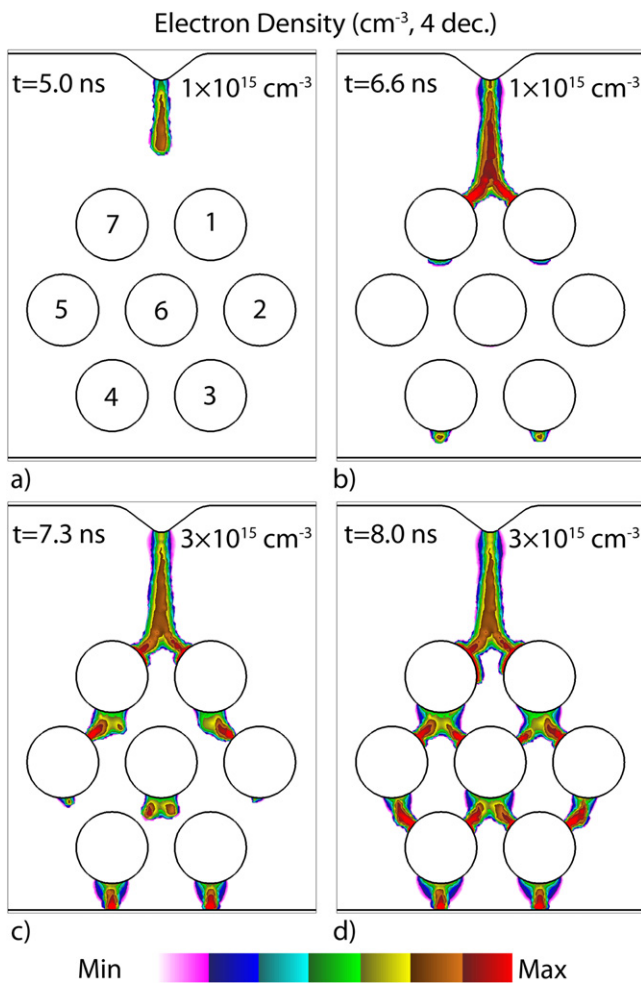


Figure 21. Time evolution of electron density in quartz lattice at 760 Torr with a +40 kV pulse. (a) 5 ns, (b), 6.6 ns, (c), 7.3 ns and (d) 8.0 ns. Log scale over 4 decades, with maximum value noted in each frame.

Discharges through air at pressures of 50, 100 and 200 Torr were simulated for quartz and zirconia disks. To approximate the ICCD imaging 2 decades of the densities of $N_2(b^1\Pi)$, the primary emitter of low-energy photons in the simulation, are shown in figure 24 for each pressure. The times for frames were chosen to show the approximate moment when breakdown occurs between all dielectric disks. The simulated emission indicates that a mode transition occurs where emission is dominated by distinct FM at high pressures to emission being dominated by volumetric and surface discharges at low pressures. In both the experiment and simulations, this transition occurs at approximately 200 Torr. With low dielectric constant—and particularly at lower pressures—the micro-discharges do not necessarily follow the vector electric field having the largest intensity. For example, with zirconia disks at 200 Torr (bottom frame in figure 24(b)), the emission from the micro-discharges is nearly normal to the surface of the disks where the electric field enhancement is largest. With quartz disks at 50 Torr (top frame in figure 24(a)), optical emission is diffuse and volumetric, or produced by SIWs.

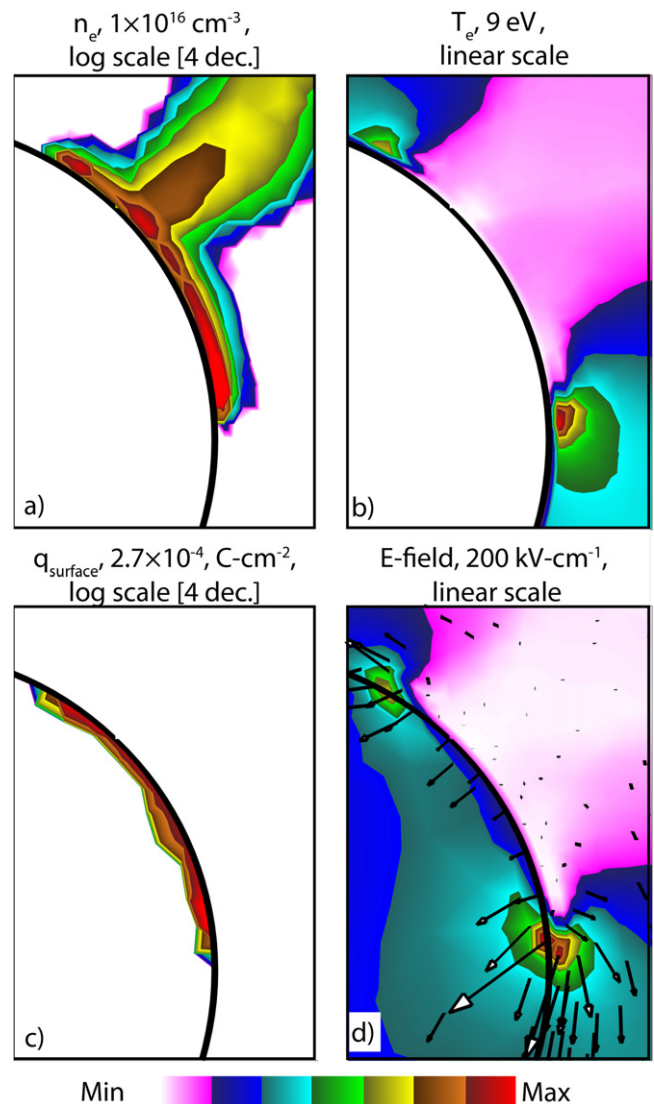


Figure 22. Plasma properties in the vicinity of disk 7 during the propagation of a surface ionization wave ($t = 8$ ns). (a) Electron density (log scale, 4 decades, $1 \times 10^{16} \text{ cm}^{-3}$ maximum), (b) electron temperature (0–9 eV), (c) surface charge (log scale, 4 decades, $2.7 \times 10^{-4} \text{ C cm}^{-2}$ maximum) and (d) electric field amplitude (contours, 0–200 kV cm^{-1}) and the electric field vectors.

At low pressures and low dielectric constant, optical emission eventually occurs in regions of relatively low electric field-enhancement—such as the void between disks 1, 7, and 6. As the pressure decreases and the mean free path of ionizing radiation increases, seed electrons are produced in regions of low electric field enhancement. Since the radiation transport is isotropic, intense SIWs can produce seed electrons behind the ionization front as well as ahead of the ionization front, thereby providing an external source of ionization in the low electric field regions. The discharges then appear more diffuse. These longer mean free paths for both radiation and charge transport result in the thickness of SIWs increasing with decreasing pressure, as shown in figure 24.

Although the optical emission appears to undergo a mode transition, closer examination indicates that the discharges

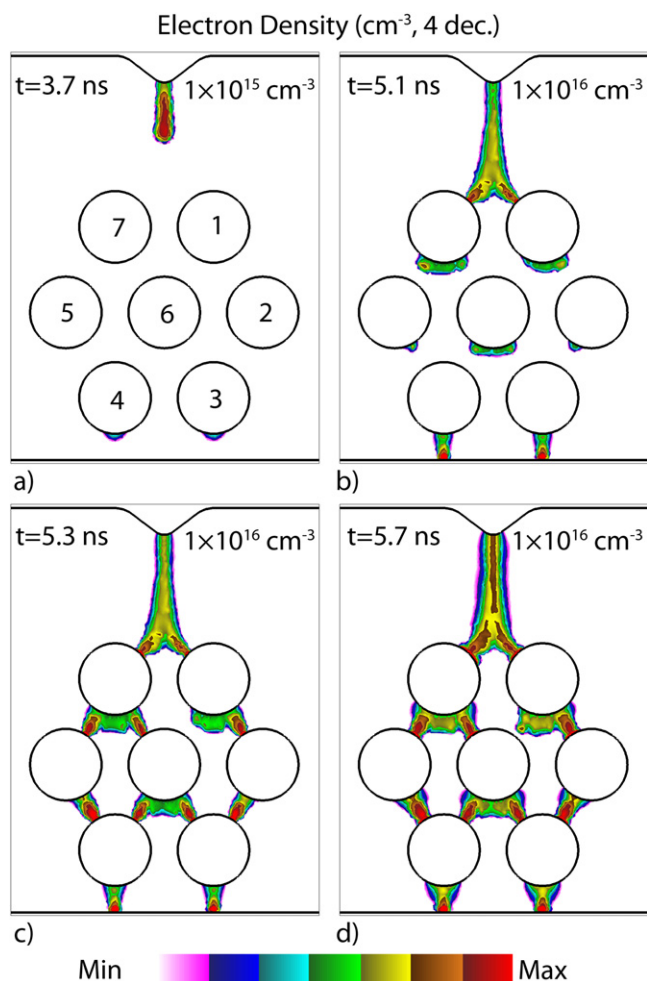


Figure 23. Time evolution of electron density in zirconia lattice at 760 Torr with a +40 kV pulse. (a) 3.7 ns, (b), 5.1 ns, (c), 5.3 ns and (d) 5.7 ns. Log scale over 4 decades, with maximum value noted in each frame.

develop in the same way regardless of pressure. For example, in figure 25 the electron density and electron impact ionization source term are shown for three times during a discharge between zirconia disks at 50 Torr. As the voltage is applied, plasma is first produced in the electric field enhanced regions between the disks—just as was the case at atmospheric pressure. However, due to the high E/N throughout the lattice and long mean free paths for electrons and ionizing photons, the ionization is not restricted to only between the gaps. Planar-like ionization waves propagate downwards throughout the lattice, similar to the initial streamers which form FM at higher pressures but less localized. The diffuse micro-discharges above the surfaces of the dielectrics have predicted electron densities of $1.1 \times 10^{13} \text{ cm}^{-3}$, with similar spatial distributions as the masked experimental images shown in figure 14. The experimental observation is that the surface discharges are far more intense at 50 Torr (see figure 14), which is corroborated by the large density of excited states shown in figure 24. When propagation of the ionization front becomes restricted to the surfaces of the zirconia disks ($t = 3.9 \text{ ns}$ in figure 25(b)), the electron densities exceed

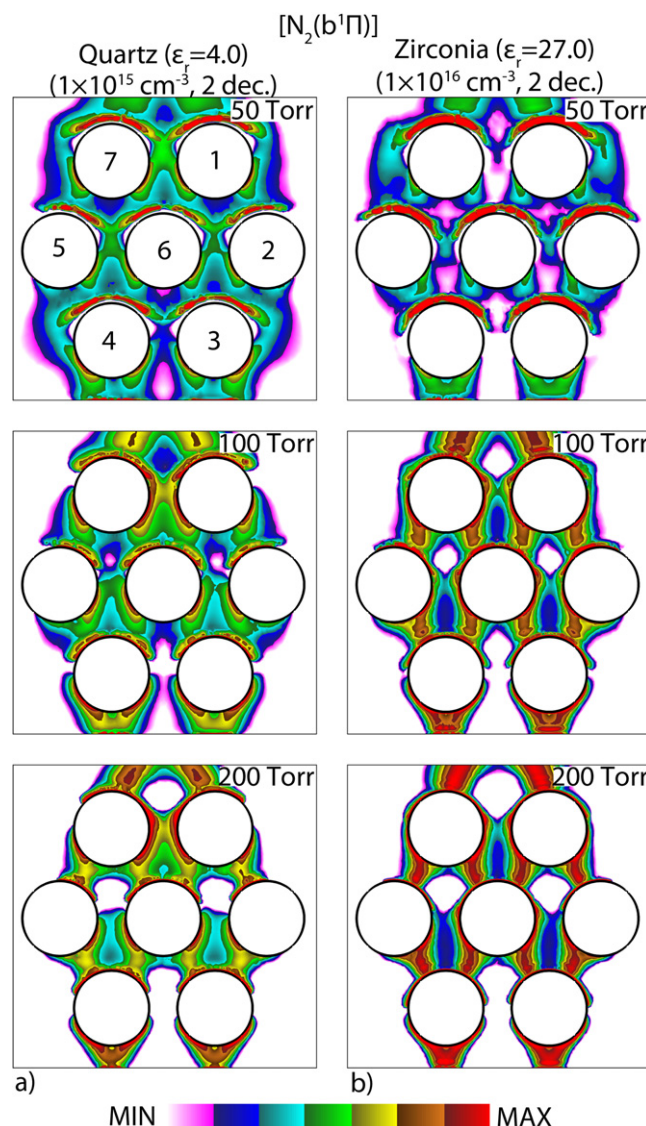


Figure 24. Densities of light-emitting species for different pressures and a 24 kV pulse with (a) quartz and (b) zirconia dielectric disks. Log scale over 4 decades with maximum value indicated in figure.

$5 \times 10^{15} \text{ cm}^{-3}$ ($t = 3.9 \text{ ns}$ in figure 25(a)). These surface regions then dominate the experimental optical images.

6. Concluding remarks

Experimental and modeling investigations of the nature of plasma formation and propagation in a 2D packed bed reactor having different dielectric packing media (quartz and zirconia) at atmospheric and sub-atmospheric pressures were performed. The discharge propagation is primarily driven by the formation of FM and SIW. In general, FM first form in the gaps between disks where electric field enhancement is greatest, which then seed SIW as the discharge propagates into surfaces. This pattern of discharge propagation dominated when using quartz disks (lower dielectric constant) at atmospheric pressure where distinct FMs clearly initiated intense SIWs. Discharges through zirconia disks (higher dielectric constant) tended to favor intense FM

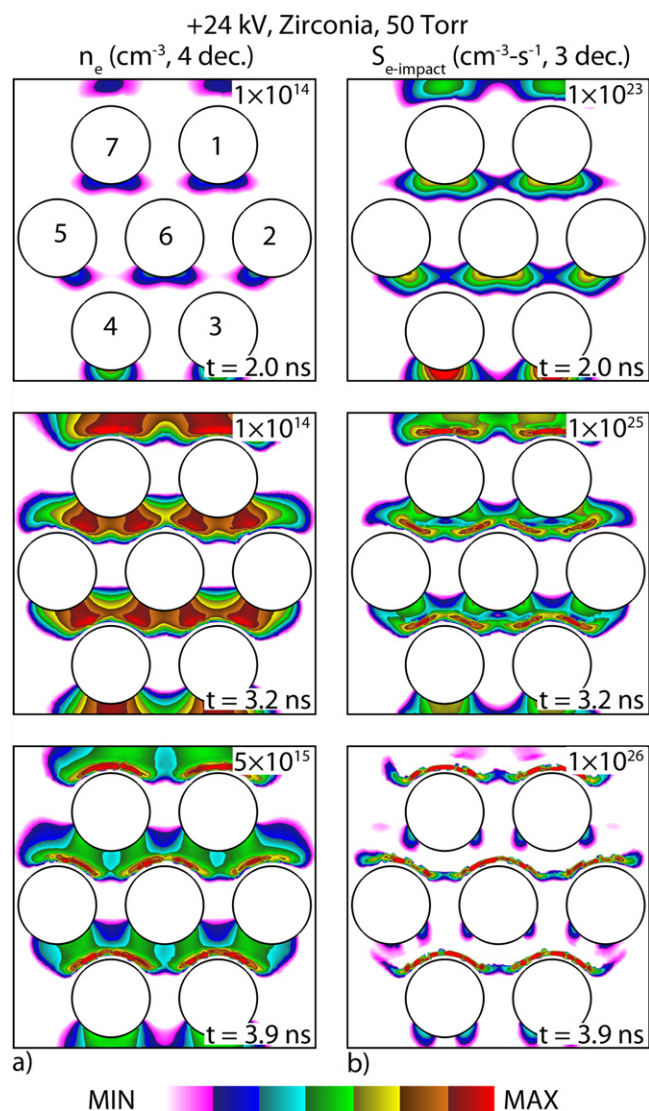


Figure 25. Evolution of a discharge at 50 Torr with zirconia disks at times shown in the figure. (a) Electron density (log scale, 4 decades) and (b) electron impact ionization (log scale, 3 decades). Maximum values are noted in each frame.

followed by weaker SIW, likely due to increased capacitance of the material. A comparison of the development of the discharges between the experiment and the model showed good qualitative agreement.

With decreasing pressure, the total plasma volume increased and particularly so in the voids between the disks. Based on the intensity of optical emission, a mode transition appears to occur approximately 200 Torr. At lower pressures, SIWs appear to dominate; at higher pressures FM dominate. By masking regions of intense emission, imaging confirmed that the FM to SIW mode of propagation occurs at all pressures, with FMs having higher intensity emission at higher pressure and SIW dominating at lower pressures. These experimental observations were also corroborated by results from the model.

This investigation used a specialized and relatively small PBR to enable both imaging and modeling. Although the physical insights that have resulted should be applicable to a wide range of conditions, the detailed results of this study are likely

only applicable to sub-regions of larger PBRs. In sufficiently large PBRs, breakdown may occur and micro-discharges form at one end of the PBR whereas a discharge may not occur at the other. The wavelike propagation observed in this investigation likely occurs regionally in the PBR but not globally. The results of this and previous studies suggest that optimizing the performance of PBRs for chemical conversion may require deliberate geometric designs beyond simply choosing the diameter and dielectric constant of spherical beads. For example, 2D-like PBRs with non-touching spherical beads would likely produce more volumetric discharges directly processing larger volumes of gas while not overly diminishing the intensity of SIWs. In those instances where microdischarges are perceived as the desired mode of operation, arranged arrays of non-spherical beads would likely be optimum.

There are certainly system issues that motivate plasma chemical processing using PBRs at atmospheric pressure. The lack of vacuum systems reduces the cost and increase the throughput, both of which are necessary for processing of low value materials. However for high valued materials, operating at lower pressures may better optimize the process. For example, in PBRs volumetric plasma chemistry occurs in the gaps and voids far from the catalysts on surfaces of the dielectrics in the form of FMs and diffuse discharges. Plasma occurs in the immediate vicinity of these catalysts in the form of SIWs. Processes may optimize with a different balance between the volumetric and surface dominated reactions. Which mode dominates discharge operation can be controlled by pressure.

Acknowledgments

This work was supported by the National Science Foundation (PHY-1519117) and Department of Energy Office of Fusion Energy Science (DE-SC0001319, DE-SC001413). We thank Michael T Lanagan of the Material Research Institute and Pennsylvania State University for supplying the zirconia disks and characterizing its dielectric constant, and Wei (Ray) Luo for his assistance.

ORCID iDs

Kenneth W Engeling <https://orcid.org/0000-0003-0408-6510>

Mark J Kushner <https://orcid.org/0000-0001-7437-8573>

John E Foster <https://orcid.org/0000-0001-8369-1828>

References

- [1] Bogaerts A, Neyts E, Gijbels R and van der Mullen J 2002 Review: gas discharge plasmas and their applications *Spectrochim. Acta B* **57** 609–58
- [2] Jiang N, Lu N, Shang K, Li J and Wu Y 2013 Effects of electrode geometry on the performance of dielectric barrier/packed-bed discharges in benzene degradation *J. Haz. Mater.* **262** 387

- [3] Mujeebu M, Abdullah M Z, Abu Bakar M, Mohamad A, Muhad R M N and Abdullah M K 2008 Combustion in porous media and its applications—a comprehensive survey *J. Environ. Manag.* **90** 2287
- [4] Chen H L, Lee H M, Chen S H and Cheng M B 2008 Review of packed-bed plasma reactor for ozone generation and air pollution control *Ind. Eng. Chem. Res.* **47** 2122
- [5] Malik M A, Ghaffar A and Malik S A 2001 Water purification by electrical discharges *Plasma Sources Sci. Technol.* **10** 82
- [6] Kraus M, Eliasson B, Kogelschatz U and Wokaun A 2001 CO₂ reforming of methane by the combination of dielectric-barrier discharges and catalysis *Phys. Chem. Chem. Phys.* **3** 294
- [7] Kim H H and Ogata A 2011 Nonthermal plasma activates catalyst: from current understanding and future prospects *Eur. Phys. J. Appl. Phys.* **55** 13806
- [8] Bogaerts A *et al* 2017 CO₂ conversion by plasma technology: insights from modeling the plasma chemistry and plasma reactor design *Plasma Sources Sci. Technol.* **26** 063001
- [9] Chung W-C, Pan K-L, Lee H-M and Chang M-B 2014 Dry reforming of methane with dielectric barrier discharge and ferroelectric packed-bed reactors *Energy Fuels* **28** 7621
- [10] Veerapandian S K P, Leys C, De Geyter N and Morent R 2017 Abatement of VOCs using packed bed non-thermal plasma reactors: a review *Catalysts* **7** 113
- [11] Butterworth T, Elder R and Allen R 2016 Effects of particle size on CO₂ reduction and discharge characteristics in a packed bed plasma reactor *Chem. Eng. J.* **293** 55
- [12] Butterworth T and Allen R W K 2017 Plasma-catalyst interaction studied in a single pellet DBD reactor: dielectric constant effect on plasma dynamics *Plasma Sources Sci. Technol.* **26** 065008
- [13] Michielsen I, Uytendhouwen Y, Pype J, Michielsen B, Mertens J, Reniers F, Meyne V and Bogaerts A 2017 CO₂ dissociation in a packed bed DBD reactor: first steps towards a better understanding of plasma catalysis *Chem. Eng. J.* **326** 477
- [14] Mei D, Zhu X, He Y, Yan J and Tu X 2015 Plasma-assisted conversion of CO₂ in a dielectric barrier discharge reactor: understanding the effects of packing materials *Plasma Sources Sci. Technol.* **24** 015011
- [15] Van Laer K and Bogaerts A 2017 How bead size and dielectric constant affect the plasma behavior in a packed bed plasma reactor: a modelling study *Plasma Sources Sci. Technol.* **26** 085007
- [16] Kang W S *et al* 2018 Surface streamer propagations on an alumina bead: experimental observation and numerical modeling *Plasma Sources Sci. Technol.* **27** 015018
- [17] Wang W, Kim H-H, Van Laer K and Bogaerts A 2018 Streamer propagation in a packed bed plasma reactor for plasma catalysis *Chem. Eng. J.* **334** 2467
- [18] Kruszelnicki J, Engeling K W, Foster J E, Xiong Z and Kushner M J 2016 Propagation of negative electrical discharges through 2-dimensional packed bed reactors *J. Phys. D: Appl. Phys.* **50** 025203
- [19] Lanagan M T, Yamamoto J K, Bhalla A and Sankar S G 1989 The dielectric properties of yttria-stabilized zirconia *Mater. Lett.* **7** 437
- [20] Hakki B W and Coleman P D 1960 A dielectric resonator method of measuring inductive capacities in the millimeter range *IRE Trans. Microwave Theory Techn.* **8** 402
- [21] Babaeva N Y, Bhoj A N and Kushner M J 2006 Streamer dynamics in gases containing dust particles *Plasma Source Sci. Technol.* **15** 591
- [22] Norberg S A, Johnsen E and Kushner M J 2015 *Plasma Sources Sci. Technol.* **24** 035026
- [23] Dorai R and Kushner M J 2003 *J. Phys. D: Appl. Phys.* **36** 666
- [24] Tsukamoto S, Namihira T, Hori H, Shinozaki K, Katsuki S and Hackam R 2001 An analysis of pulsed streamer discharge using a high-speed camera *Proceedings of Pulsed Power-Plasma Science (Las Vegas, USA)*